Master's thesis
Department of Geoscience and Geography
Solid Earth Geophysics

MAGNITUDES ESTIMATED WITH DIFFERENT STATION TYPES OF THE NETWORK MONITORING THE 2018 GEOTHERMAL RESERVOIR STIMULATION IN ESPOO, SOUTHERN FINLAND

Eemil Arola

11/2020

Supervisor:

Gregor Hillers (University of Helsinki)

UNIVERSITY OF HELSINKI
FACULTY OF SCIENCE
MASTER'S PROGRAMME IN GEOLOGY AND GEOPHYSICS

PL 64 (Gustaf Hällströmin katu 2)

00014 Helsingin Yliopisto

HELSINGIN YLIOPISTO
HELSINGFORS UNIVERSITET
UNIVERSITY OF HELSINKI
MATEMAATTIS-LUONNONTIETEELLINEN TIEDEKUNTA
MATEMATISK-NATURVETENSKAPLIGA FAKULTETEN
FACULTY OF SCIENCE

Tiedekunta – Fakultet – Faculty	Koulutusohjelma – Utbildningsprogram – Degree programme
Faculty of Science	Master's programme in Geology and Geophysics

Opintosuunta – Studieinrikting – Study track

Solid Earth Geophysics

Tekijä – Författare – Author

Eemil Juhani Arola

Työn nimi – Arbetets titel – Title

Magnitudes estimated with different station types of the network monitoring the 2018 geothermal reservoir stimulation in Espoo, Southern Finland

Työn laji – Arbetets art – Level	Aika – Datum – Month and year	Sivumäärä – Sidoantal – Number of pages
Master's thesis	11/2020	75 p. + 5 p. appendix

Tiivistelmä – Referat – Abstract

The ST1 Deep Heat company has been developing an enhanced geothermal system for district heating in Espoo, Southern Finland by St1 Deep Heat Company. Complete project will consist of geothermal doublet which involves two wells expanding up to 6,1 km depth. The stimulation of the first well was conducted in summer of 2018 as a 7-week period during which the fluid permeability of the crystalline rock at the base of the well was increased by pumping water with high pressures into the well. The stimulation process interacts with the ambient stress field of the subsurface and similar processes have been associated with induced seismicity when the stress changes lead into earthquakes as pre-existing faults and cracks are activated and new ones are created.

For the monitoring of the seismic activity associated with the project a seismic network was installed in the Espoo/Helsinki area. The network consisted of 12 borehole installed 3-component seismometers provided by ST1 Deep Heat Company and from 5 semi-permanent surface 3-component broadband seismometers and in total 100 geophones installed by the Institute of Seismology, University of Helsinki (later ISUH). The geophones were installed in 3 large 25-instrument arrays, 3 smaller 4-instrument arrays and as single stations. Data from suitable seismic stations from the Finnish Seismological network was also used in the study.

The aim of the study was to map possible differences and trends in the determined event magnitudes between different types of seismic stations used in the seismic network during the stimulation. The effect of different filter choices on amplitude measurement is also studied and discussed for some of the seismic events involved in the study. The results are also compared to the traffic light system warning thresholds of the EGS project and automatically calculated magnitudes of the monitoring system. The Finnish local magnitude formula is also discussed considering near-source events. Reliability and behaviour of the seismic arrays used during the stimulation is studied and discussed. Azimuthal effects noted during the data processing are illustrated. According to the results there appears to be clear differences in estimated magnitudes between the different station types used in the network and differences and trends between the seismic arrays and between individual instruments of single arrays.

In total 21 induced events were chosen based on their automatically determined magnitudes, favouring events with large as possible magnitudes. Magnitude range for the events was from M_L 1.8 to M_L 1,0. The events were picked for P- and S-wave arrivals and for amplitudes estimated from vertical component S-wave arrivals. The locations and magnitudes of the events were determined using the currently used practices of the ISUH. Main tools used in the study are the Geotool software for waveform analysis, an ISUH program used for earthquake locating and GNU Octave programs written by the author used in the data procession.

Avainsanat – Nyckelord – Keywords

Induced earthquakes, reservoir stimulation, enhanced geothermal system

Säilytyspaikka – Förvaringställe – Where deposited

Helda- Digital repository of the University of Helsinki

Muita tietoja – Övriga uppgifter – Additional information

HELSINGIN YLIOPISTO
HELSINGFORS UNIVERSITET
UNIVERSITY OF HELSINKI
MATEMAATTIS-LUONNONTIETEELLINEN TIEDEKUNTA
MATEMATISK-NATURVETENSKAPLIGA FAKULTETEN
FACULTY OF SCIENCE

Tiedekunta – Fakultet – Faculty	Koulutusohjelma – Utbildningsprogram – Degree programme
Matemaattis-luonnontieteellinen tiedekunta	Geologian ja geofysiikan maisteriohjelma

Opintosuunta – Studieinrikting – Study track

Kiinteän maan geofysiikka

Tekijä – Författare – Author

Eemil Juhani Arola

Työn nimi – Arbetets titel – Title

Magnitudes estimated with different station types of the network monitoring the 2018 geothermal reservoir stimulation in Espoo, Southern Finland

Työn laji – Arbetets art – Level	Aika – Datum – Month and year	Sivumäärä – Sidoantal – Number of pages
Pro gradu	11/2020	75 s. + 5 s. liitteitä

Tiivistelmä – Referat – Abstract

ST1 Deep Heat Oy on rakentanut parannettua geotermistä järjestelmää Espooseen. Projektin tarkoituksena on tuottaa geotermistä lämpöä lämmitystä varten. Valmistuessaan projekti koostuu kahdesta yli 6 kilometrin syvyyteen ulottuvasta reiästä, joiden kautta vettä kierrätettäisiin kallioperässä. Ensimmäisen reiän stimulaatio aloitettiin vuoden 2018 kesällä 7 viikkoa kestäneellä jaksolla, jonka aikana vettä pumpattiin kovalla paineella reikään sen pohjalla olevan kallion permeabiliteetin kasvattamiseksi. Stimulaatioprosessi vaikuttaa maanalaiseen jännityskenttään ja vastaavissa projekteissa on havaittu indusoitunutta seismisyyttä johtuen jännitystilan muutoksista, jotka aktivoivat ennestään olemassa siirroksia ja rakoja ja synnyttävät uusia.

Projektin monitorointia varten Espoon ja Helsingin alueelle asennettiin seisminen valvontaverkko. Kokonaisuudessaan verkko koostui 12 kairareikiin asennetusta 3-komponenttisesta seismometristä, jotka ST1 Deep Heat Oy asensi sekä viidestä puoliksi pysyvästä pinnan lähelle asennetusta 3-komponenttisesta laajakaista seismometristä ja yhteensä noin 100:sta geofonista, joiden asentajana toimi Helsingin yliopiston Seismologian instituutti. Geofonit asennettiin kolmena suurempana 25 instrumentin joukkona, kolmena pienempänä neljän instrumentin joukkona sekä yksittäisinä instrumentteina. Tutkimuksessa hyödynnettiin mahdollisuuksien mukaan myös Suomen seismisen asemaverkon pysyviä asemia.

Tutkimuksen tarkoituksena oli kartoittaa mahdollisia eroja erilaisten ja eri tavoin asennettujen seismisten asemien magnitudimääritysten kesken. Myös erilaisen seismisen datan suodattamisen vaikutusta määritettyihin amplitudeihin tutkittiin osalle tutkimuksessa käytetyistä maanjäristyksistä. Tuloksia verrattiin myös stimulaatioprosessin valvontaan käytetyn automaattisen liikennevalojärjestelmän hälytysrajoihin. Tällä hetkellä käytössä olevan Suomen lokaalin magnitudiasteikon sopivuutta arvioitiin tutkimuksessa esiintyneille seismisille lähitapauksille. Geofonijoukkojen luotettavuutta ja sisäisiä eroja arvioitiin. Myös tutkimuksessa havaittuja määritettyjen magnitudien atsimutaalisia eroavaisuuksia havainnollistetaan kartalla. Saatujen havaintojen perusteella voidaan todeta, että on olemassa selviä eroja ja trendejä monitorointiverkon eri asematyyppien välillä määritettyjen magnitudien suhteen sekä yksittäisen geofonijoukon sisäinen vaihtelu määritettyjen magnitudien suhteen voi olla keskimäärin suurta.

Kokonaisuudessaan 21 indusoitua maanjäristystä valittiin tutkimusta varten niiden automaattisesti määritettyjen magnitudien perusteella, suosien mahdollisimman suuria tapauksia. Tapausten magnitudien vaihteluväli oli välillä 1,8:sta 1,0:aan lokaalilla magnitudiasteikolla. Kaikille tapauksille määritettiin P- ja S-aaltojen saapumisajat sekä amplitudit mittaamalla S-aallon vertikaalikomponenteista. Tapauksien paikat ja magnitudit määritettiin tällä hetkellä käytössä olevien Seismologian instituutin metodien mukaisesti. Pääasialliset tutkimuksessa käytetyt työkalut olivat Geotool-ohjelma aaltomuotojen analysointia varten, Seismologian instituutin paikannusohjelma maanjäristyksille ja tekijän itse kirjoittamat ohjelmat GNU Octavella, joita käytettiin datan prosessointiin.

Avainsanat – Nyckelord – Keywords

Induced earthquakes, reservoir stimulation, enhanced geothermal system

Säilytyspaikka – Förvaringställe – Where deposited

Helda- Helsingin yliopiston digitaalinen arkisto

Muita tietoja – Övriga uppgifter – Additional information

Table of contents

1 INTRODUCTION

ST1 Deep Heat is an enhanced geothermal system being developed in Espoo, Southern Finland. The project is located in a densely populated area with heavy infrastructure quite near Finland's capital city Helsinki. The goal of the project is to provide geothermal heat for local district heating. Complete project will consist of a geothermal doublet which involves two wells expanding up to 6,1 km depth. The stimulation for the first well drilled (OTN-3) was conducted in summer of 2018 as a 7-week period during which the fluid permeability of the crystalline rock at the base of the well was increased by pumping water with high pressured into the well. Such actions interact with the ambient stress field of the subsurface and have been associated with induced seismicity when the stress changes lead into induced earthquakes as pre-existing faults and cracks are activated and new ones are created.

For the registering and surveillance of the seismic activity associated with the project a seismic network was installed in the Espoo and Helsinki area. The network consisted of 12 borehole installed 3-component seismometers provided by ST1 Deep Heat Company and from 7 semi-permanent surface 3-component broadband seismometers and in total 100 geophones installed by the Institute of Seismology of University of Helsinki (later ISUH). The instruments listed are located within 10km radius of the stimulation well. In addition to the mentioned seismic network, suitable stations from the Finnish National Seismic Network were also used in the study.

The aim of the study was to assess the reliability of the magnitude determinations with the current methods available in the routine analysis at the ISUH and to map possible differences and trends in the determined magnitudes between different types of seismic stations and arrays of the used seismic network. The suitableness of the currently in use magnitude formula of the Finnish local magnitude scale is also assessed for this kind of near source events. The reliability of the magnitude measurements is of great importance for an earthquake inducing project located near residential areas or delicate infrastructure in order to reduce the possible dangers and nuisances associated with the project, therefore affecting the viability of such a project.

This study was done by selecting in total 21 events based on the automatically determined magnitudes, favouring events with as large as possible magnitudes. Largest magnitude event was M_L 1,8 whereas the smallest events corresponded roughly to M_L 1,0. The events were manually picked for P- and S-wave arrivals and for amplitude records. The locations and magnitudes of the events were determined using the currently in use practices of the ISUH. Main tools used in the study alongside the instruments used to gather the data are Geotool software used in waveform analysis, a ISUH program used for locating seismic events in routine seismic analysis and GNU Octave programs written by the author used in procession of the data and illustration of the results.

2 SEISMIC WAVES

2.1 BODY AND SURFACE WAVES

Scientific study of earthquakes is largely based on understanding the propagation of the seismic waves through the subsurface. The propagation is controlled by the elastic properties of the medium. The theory behind the seismic waves is described more precisely in Shearer (1999), Lay (1995) and Bormann (2012). The background theory provided below will help to understand the behavior of the seismic waves and their most important properties.

The two most essential types of the seismic waves are the P- and S-waves. These two wavetypes are the fundamental mechanical waves that propagate through the interior of a solid medium. The existence of these waves can be related to the equations of motion and the elastic constitutive laws. P-waves are compressional mechanical waves that involve changes in both the volume and the shape of the medium. The S-waves involve only shearing deformation and involve no disturbance in the volume. As a result S-waves can't propagate in fluids since fluids can't sustain shear stresses. Often these two types of seismic waves are together referred to as body waves. The commonly used notations P and S come from the words primary and secondary waves. The primary waves have higher propagation velocity than the secondary waves and therefore arrive first from any source when considering an elastic solid material. The particle motions for the P- and S-waves are shown in figure 2.1.

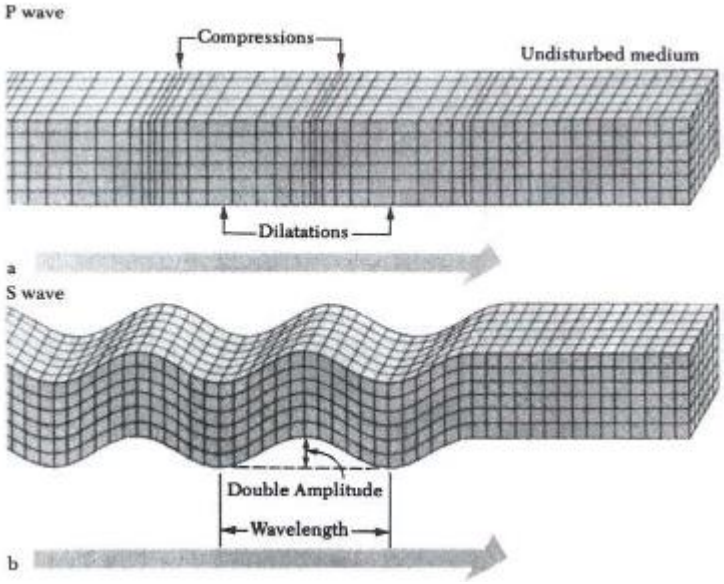

Figure 2.1 Particle motions involved in passage of the two fundamental seismic waves: the P-wave and the S-wave. The waves are propagating from the left to the right. As can be observed from the figure the P-wave involves both a volume change and a change in shape whereas the S-wave includes only a change in shape and involves no volume change. The relative changes caused by the propagating wave have been exaggerated greatly in the figure. This figure is modified after Lay (1995).

In addition to the P- and S-waves there also exists other wave types for solid elastic material involving free surfaces. There are two distinct types of these surface waves which are the Rayleigh and the Love waves. These wave types result from the interaction of the body waves with a free surface. The surface waves tend to have slower propagation velocities than the body waves. For Love waves to be formed it is also required to have a wave velocity increase with depth, which tends often to be true for the real Earth. For Rayleigh waves this is not required since they can exist in homogenous half-space. Since the surface waves are not used in the study they will not be discussed in a greater extent. The particle motions for the surface waves are shown in figure 2.2.

The propagation of the seismic waves mentioned is affected by the elastic parameters and changes in material properties in the medium they are traveling in. The behaviour of the seismic waves and their particle motions will be next discussed further.

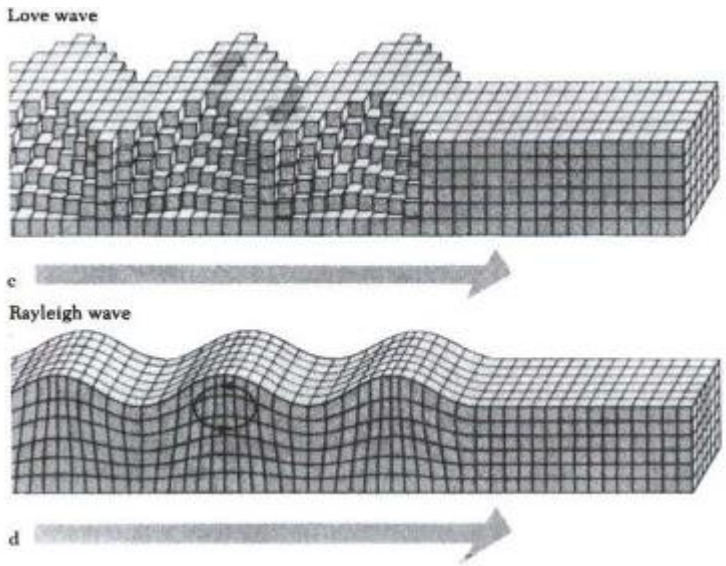

Figure 2.2 Particle motions involved in passage of the surface waves: the Love wave and the Rayleigh wave. The waves are propagating from the left to the right. As can be observed from the figure the Disturbance tends to be at it's maximum at the surface and diminish downwards. The relative changes caused by the propagating wave have been exaggerated in the figure. This figure is modified after Lay (1995).

The propagation velocities of the P- and S-waves can be expressed as:

$$V_P = \sqrt{\frac{\lambda + 2\mu}{\rho}} \qquad (1)$$

for P-wave and:

$$V_S = \sqrt{\frac{\mu}{\rho}} \qquad (2)$$

for the S-wave, where λ is the first Lame parameter, μ is the shear modulus and ρ is the medium density.

The relationship may differ to some extent in the real world when the medium is not an ideal Poisson solid, though this relationship almost holds for igneous and consolidated sediment rocks in the Earth's crust. As can be observed from the formulas (1) and (2) the elastic parameters of the medium determine the travel velocity of the seismic body waves.

The differences in the velocities of the body waves can be used when estimating the distance from the seismic source at a receiver. As a general rule one could say that the velocities of the seismic waves increase when going deeper down the crust from the surface.

As harmonic waves the body and surface waves also involve several other parameters related to the wave motion. A mechanical wave can be characterized based on its period, frequency, angular frequency, wavelength and wavenumber in addition to the propagation velocity. The parameters can quite easily be calculated from each other if others of them are known. One important and often used parameter considering the seismic waves is the amplitude, which expresses the maximum displacement of a particle in the medium from its rest position.

In seismology the amplitude is an important quantity of a seismic wave since many methods used for quantifying earthquake sizes require knowing the amount of the medium displacement at a certain location. This is because seismic events with more energy release tend to cause seismic waves causing higher displacements in the medium, therefore having higher amplitude. However there are several phenomena affecting the amplitude records which will be discussed later in this section.

2.2 SEISMIC RAYS

For understanding how the seismic waves travel in the Earth the concept of seismic rays is often used in seismology. When a seismic wavefield is represented as rays it brings new useful concepts such as

wave arrivals and seismic phases. The idea of a seismic ray is that the arrival corresponds to a transient disturbance that has propagated along a path that can be defined between the receiver and the seismic source. This so called arrival consists of two parameters: amplitude and travel time. These mentioned parameters can be quantified by using the Eikonal equation.

The path of the seismic ray in the elastic medium is affected by the changes in the wave's velocity in different parts of the medium. Now also a parameter called angle of incidence is required. It corresponds to the angle between the ray and the interface of the zones with different wave velocities.

By using fairly simple ray geometry and Fermat's principle one can derive Snell's law:

$$\frac{\sin i_1}{\sin i_2} = \frac{v_2}{v_1} \qquad (3)$$

Where i_1 is the angle measured from the normal of the boundary in material one, i_2 is the corresponding angle for the material two and v_1 and v_2 are the corresponding wave velocities in the materials. The law can be used to understand how the ray behaves when facing a velocity boundary. Snell's law is familiar from optics but it also applies to seismic rays. Snell's law can be generalized as

$$\frac{\sin i}{v} = p \qquad (4)$$

Where i is the inclination angle, v is the changed velocity and p is called ray parameter. When a ray enters material with higher wave velocity the ray is deflected towards the horizontal. In opposite situation it is deflected towards the vertical. If $p = 0$, the wave is travelling vertically and no deflection will be experienced.

Figure 2.3 shows the behaviour of seismic rays with changes of velocity with depth. The behaviour of the seismic ray leads to curvature of the ray's path in a medium having a velocity gradient.

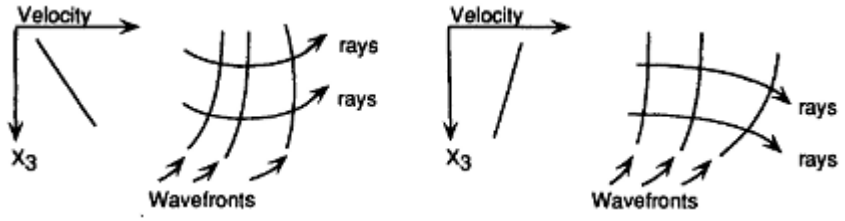

Figure 2.3 The seismic rays experience curvature when encountering a medium with a velocity gradient. The direction of the curvature is related to the gradient. This figure is Adapted from Lay (1995).

2.3 AMPLITUDE AND GEOMETRICAL SPREADING

The amplitude of the seismic arrival at a receiver is greatly affected by how the seismic wave propagates in the medium. The wave can be considered to be spherical and therefore when traveling through the medium the wave expands and therefore the wave's energy is divided into an expanding area. Considering the wave traveling a small distance from the source and the changes in velocity to be negligible, the energy of the mechanical disturbance is now distributed on a spherical wavefront for a point source (the most simple case).

When the spherical wavefront expands as it travels further in the medium as the time passes, the same total energy will be distributed into a larger area. Since the total energy is constant, the energy per unit of area decreases as the wavefront expands further. If we define the total energy of the wavefront as E_{total} then the energy per unit area becomes $E_{total}/2\pi r^2$ where $2\pi r^2$ is the area of the spherical wavefront with radius of r. The effect mentioned can be addressed as geometrical spreading. As a simple rule the energy density and the amplitude of the seismic wave can be related to the traveled distance as follows:

$$E \approx \frac{1}{r^2} \tag{5}$$

$$A \approx \frac{1}{r} \tag{6}$$

However when considering the chance of the velocity with depth in the medium, the situation becomes a bit more complicated since the seismic waves tend to refract when traveling through a medium with a velocity gradient. Other effects causing decay in the arrival's amplitude are the partitioning of the seismic energy at boundaries, seismic diffraction, attenuation and scattering.

2.4 PARTITIONING OF SEISMIC ENERGY AT A BOUNDARY

When encountering an interface between two mediums with different wave propagation velocities a wave refracts or reflects. As a notice α is often used as the velocity of the P-wave in the medium and β is used as the velocity of the S-wave. When considering the process more precisely in fact when P- or SV-wave meets the boundary in total four derivative waves are excited. First is the refracted or transmitted P-wave. Second is refracted SV (which is generated if $\beta_2 > \alpha_1$). Third is the reflected P-wave and fourth is the reflected SV-wave. The overall ray geometry these waves exhibit is governed by Snell's law. The ray parameter p is constant for all the waves. In case of the SH-wave only two waves are generated in similar situation with the boundary: reflected and refracted SH waves. The existence of these waves means that the energy must be partitioned along the rays.

The behaviour of the P-wave wave encountering a velocity discontinuity is illustrated in figure 2.4.

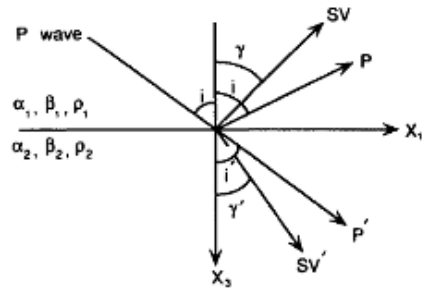

Figure 2.4 The P-wave encounters a solid-solid surface and generates additional waves. The angles are determined by the medium properties. This figure is adapted from Lay (1995).

The angles of the rays after meeting a velocity discontinuity can be determined from Snell's law according to:

$$\frac{\sin i}{\alpha_1} = \frac{\sin \gamma}{\beta_1} = \frac{\sin i'}{\alpha_2} = \frac{\sin \gamma'}{\beta_2} \qquad (7)$$

where α and β correspond to the velocities of the P- and S-waves in the mediums 1 and 2 and i and γ correspond to the angles of incidence associated with the interface of the mediums.

Next the partitioning of the amplitudes will be discussed in the case of the previous situation. The amplitude partitioning can be understood using reflections and transmission coefficient, which are related to the acoustic impedances across the interface. The acoustic impedance is related to the elastic properties of the material such as density and the body wave velocities. The transmission and reflection coefficient for different wave partitioning will not be listed here but they can be found in Lay (1995) in table 3.1.

2.5 ATTENUATION AND SCATTERING

In a case of an ideal, perfectly elastic Earth the geometrical spreading, reflection and refraction of the seismic wave would control the amplitude decay. This however is not completely the case with the real Earth. In the real Earth the waves attenuate with time because of several mechanisms which cause them to lose energy in addition to the geometrical spreading. As the wave propagates it converses potential energy (particle position) to kinetic energy (particle velocity). This conversion is not completely reversible. In the process other work is done involving movement along mineral

dislocations and heating of grain boundaries caused by shear. These processes consume some of the seismic wave's energy. These types of processes can be called collectively as internal friction. The formulas modeling these effects however must be greatly simplified since the individual effects are very complex. These effects can be considered to some extent by thinking about an oscillating mass on a spring, which loses some of its energy per cycle.

This leads into exponential decay of oscillation. A quality factor, marked often with Q, can be used to describe fractional loss of energy per cycle of oscillation.

As a formula the effect can be expressed as:

$$\frac{1}{Q} = \frac{-\Delta E}{2\pi E} \qquad (8)$$

where Q is a value describing the energy loss per cycle, E is the total energy and ΔE is the energy loss per cycle.

Since the energy loss is tied to the frequency of the cycles it leads to the observation that the higher frequency seismic waves attenuate faster. This leads in removal of higher frequency content from seismic arrivals at greater distances since the higher frequencies are more effectively dampened by the attenuation. It also appears that the Q-values differ for P- and S-waves in real Earth. The S waves appear to attenuate faster, this could be caused by shear motion. On average competent rocks with higher seismic wave velocities and densities have higher Q-values, in other words they attenuate waves less.

As a notice most of the receivers used in this study are quite near the source of the seismic waves so the high frequency content most likely has not attenuated as much as it usually would when using permanent seismic station network with often much greater source-receiver distances.

2.6 SITE AMPLIFICATION OF AMPLITUDE

When considering the arrival amplitude at the receiver it also should be noted that the medium properties affect the measured amplitude. Such effect is known as the site amplification and it can increase the amplitude of the seismic wave when it comes from more rigid and dense medium into less rigid and less dense material near the receiver. If the receiver is located in an area experiencing high site amplification the measured amplitudes are amplified. Of course the increased amplitude in

this case does not mean that the energy of the seismic wave has somehow increased, instead the increase in amplitude is experienced since the medium of the high site amplification area requires less energy to be "moved". Therefore in this case the increase in the amplitude is related to the material properties.

2.7 TRAVEL TIMES IN A LAYERED EARTH MODEL

Quite often in seismic models the standard method is to create the velocity structure of the Earth by using layers with different seismic wave velocities instead of having a continuous velocity gradient. The travel times of the seismic phases can be fit as function of distance with the laterally homogenous layered model. When the ray arrives at a boundary between two layers with different velocities it is partitioned between refracted and reflected rays. These new rays have the same ray parameter as the ray from which they originated. The angles of these two rays are calculated using Snell's law equation (3) mentioned in section 2.2 in this chapter. In some cases Snell's law predicts a critical reflection which is experienced when the wave travels horizontally between the layers immediately below the second layer. This kind of wave is often called as a head wave and it transmits energy back into the upper layer as it travels through the interface. The energy leaves the boundary at the incidence angle (critical angle in this case) which can be expressed as $i_c = \sin^{-1}(v_1/v_2)$. The indexes 1 and 2 are related to the upper and lower layer. If the incidence angle is greater than the critical angle ($i < i_c$), then all of the energy is reflected back into the upper layer at the interface. Though if $v_2 < v_1$ then the critical angle does not exist. In that case the refracted wave deflects towards the vertical. The different paths the waves can take and the reflections and refractions are illustrated in figure 2.5.

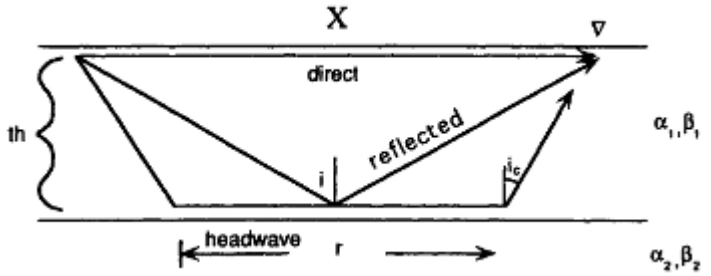

Figure 2.5 The behaviour of the seismic rays in a model with layers having different wave velocities. The three most principal types of the rays are named in the figure. This figure is adapted from Lay (1995).

The theoretical travel times for this case can be quite easily calculated for both the sources on surface and for the sources inside the layers when knowing the angles and the wave velocities based on simple algebra and trigonometry. As a note at close distances only direct and reflected wave arrivals exist. If the receiver is too close to the seismic source the refracted wave does not arrive at it as can be observed from the figure 2.5.

The first arrival from the source to the receiver changes based on the distance from the source. At closest distances the direct arrival from the source to the receiver arrives in the shortest time. At critical distance X_c the refracted wave reaches the direct wave and from that point it will be the first arrival. Since the reflected wave travels greater distance but does not benefit from the greater velocity of the layer below it won't be the fastest arrival at any distance.

It should be mentioned that dipping velocity layers complicate the calculations further and affect the travel time curves. The behaviour of the arrival times as function of distance can be seen in figure 2.6.

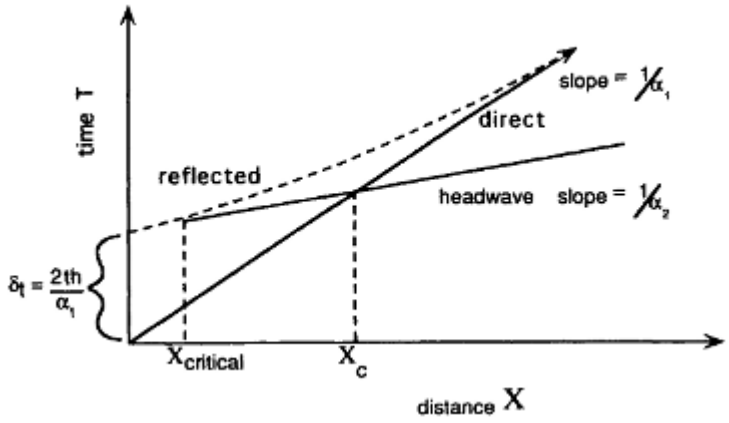

Figure 2.6 Travel times of the seismic rays corresponding to the model of figure 2.5. As can be observed from the figure the first arrival changes related to the distance from source. This figure is adapted from Lay (1995).

Since in the study the area is reasonably small compared to the scale of the Earth the travel times in spherical Earth will not be discussed because it is much simpler to make the calculation considering a flat layer while the approximation is still viable. Most of the arrivals of the seismic phases used in the study are caused by direct arrivals because of the relatively small source-receiver distances. Layered model with many layers is mostly required only for some further away permanent station records in the scope of this study.

2.7.1 Explosion, the least complicated type of a seismic event

Since an ideal explosion is theoretically the least complicated type of a seismic event, it will be used as an example before continuing deeper into earthquakes. In theory an explosion is expected to create outwards directed compressional first motion in any direction it is observed from. Compared to earthquake for which the whether the first motion is compressional or dilational is related to the focal mechanism and from which direction the earthquake is observed. The concept of focal mechanism will be discussed further in the section 2.8. When comparing an explosion with an earthquake the duration of the source and rise time to the maximum amplitude tend to be shorter than with real earthquakes. The energy spectrum of an explosion is more shifted to higher

frequencies when comparing with earthquakes. As a conclusion an explosion should in theory radiate energy uniformly in all directions, however the medium anisotropy may still result in differences when observing at receivers at different locations. Figure 2.7 shows energy radiation pattern of a theoretical explosion.

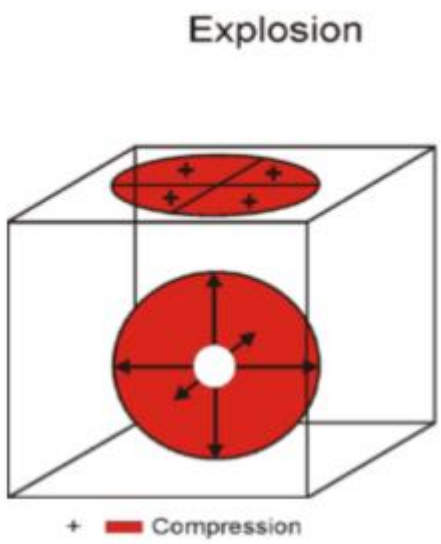

Figure 2.7 Theoretical energy radiation pattern of an explosion. It should be noted that the first particle motion is positive in all directions from the source. This figure is adapted from Bormann (2012).

2.8 EARTHQUAKES

Tectonic earthquakes are a result of the brittle part of the Earth's crust being affected by stress which exceeds its breaking strength. In this kind of situation, a sudden rupture is experienced during which part of the stored energy is released as seismic waves. The rupture happens often along pre-existing areas of structural weakness such as faults, but sometimes the rupture can happen along newly formed fault. It could be said that the material on the opposite sides of the rupture "snaps" into the new position. The size of the rupture tends to scale upwards with increasing earthquake size.

The rock breaking strength is affected by the confining pressure, rock mechanical parameters (affected by composition and fabric such as grain size and anisotropy and such), porosity and temperature. Rock strength tends to be higher under compressive stress than under tensional stress. If the rock is pre-fractured the breaking strength is lowered even further. In the case of a pre-fractured rock the strength is mostly controlled by the frictional resistance of the opposite sides of the fault. This depends on the orientation and the stress field alongside few other conditions.

The required stress for the tectonic earthquakes is generated mostly by the motions of the lithospheric plates relative to each other. Depending on the area and situation there can also be

some other contributing factors to the seismicity such as isostatic uplift caused by glacier melting and pumping or removal of fluids into the rock as result of human action.

Most of the earthquakes occur near the boundaries of the lithospheric plates. However in the case of this study the earthquakes in the area are intraplate and induced by human action.

As such they are located far from the boundaries between lithospheric plates. The intraplate seismicity is mostly located in the upper crust. In Fennoscandia great majority (80%) of the natural seismic activity is located in the uppermost 17 km of the crust. Only 19 % of the naturally occurring seismic events take place in the middle crust (17-31 km deep) and only 1 % deeper than that in the lower crust (Korja & Kosonen 2015). According to Bormann (2012) intraplate natural earthquakes contribute less than 5% of the annual seismic moment release of the whole Earth.

Tectonic earthquakes are often associated with several different types of faulting mechanisms: strike-slip, thrust and normal faulting. The faulting mechanism can also be combination of the mentioned types. The relative movement of the sides of the fault causes the seismic waves to radiate differently into different directions. In some directions the P-wave is at maximum amplitude and in some directions it theoretically is not radiated at all. The same applies for the S-wave, but in 45 degree angle compared to the P-wave. The polarity of the first arrival also changes per 90 degree shift in direction. Figure 2.8 illustrates the seismic wave formation in the case of a strike-slip earthquake.

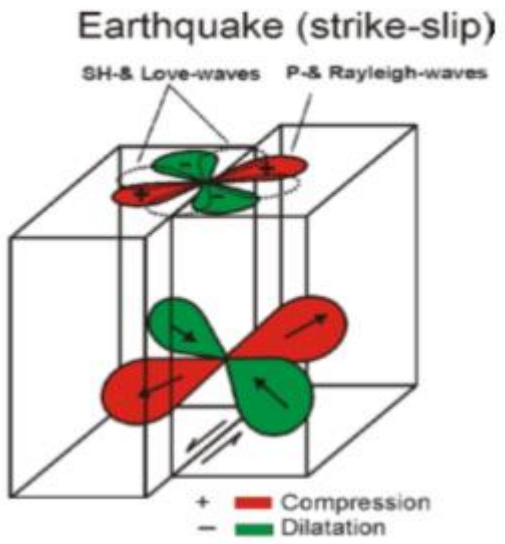

Figure 2.8 Idealized strike-slip earthquake along a vertically dipping fault. Positive polarities are marked with red color and negative polarities are marked with green. The patterns show the dependence of the amplitude relative to the azimuth. This figure is adapted from Bormann (2012).

When considering the energy released by an earthquake it should be noted that from the total available elastically stored energy most of it is required in the growth of the fracture. Energy is also

lost into frictional heat, sound and to other phenomena. A reasonably small fraction of the total energy is used to produce the seismic waves. The efficiency of the wave creation depends on many factors such as stress drop, total stress of the region and the medium properties.

2.9 MAN-MADE SEISMIC EVENTS

Alongside the tectonic earthquakes some seismic events can be classified as man-made. Events such as explosion and induced earthquakes can be caused by human actions. There are also few other man-made event types, but they are of no interest to this study.

The induced seismicity can be divided into several classes, but mostly the unifying factor between them is that the human action somehow changes the stress state of the rock medium. The changes in ambient stress or pore pressure in the medium exceeding its breaking strength and therefore causing an earthquake.

2.9.1 Induced seismic events

Considering the subject of this study, the most essential type of the induced events are the earthquakes induced by injecting fluid into the rock and therefore increasing pore pressure and possibly affecting stress state enough to trigger earthquakes.

Typically the magnitudes of the induced events tend to be smaller than the largest events occurring naturally in the area. When considering the earthquake as physical process the induced earthquakes are not distinguishable from the natural ones. However since human action is often restricted to somewhat shallow depths the induced events often take place at shallower depths when compared to natural events.

There are several mechanisms which can lead into an induced earthquake. These include changes in pore pressure, earthquake-earthquake interactions, deformation related changes, temperature changes and chemical alterations.

In pore pressure change the pore pressure of a pre-stressed fault is increased by fluid injection and it can cause the fault to rupture therefore releasing stored tectonic stress. Other way to change the pore pressure is to pump fluid out of the reservoir but according to Hirschberg et. al. (2015) the reduction of pore pressure often results in stabilization instead of induced seismicity.

In earthquake-earthquake interaction the static and dynamic stress changes caused by the induced earthquakes themselves trigger additional earthquakes.

Deformation related changes are related to injected or extracted fluid or in some cases material extraction by mining which affects the local stress field and might therefore trigger ruptures on nearby faults. When the local loading exceeds the elastic strength an earthquake will be induced.

Temperature changes such as cooling or heating of rock material caused by injected fluids results in local thermal contraction or expansion. This affects the mechanical properties of the local area by opening fracture apertures. Thermo-elastic deformation also causes local perturbations in the stress-state.

In some cases chemical alteration is caused by injected fluid. In chemical alteration clay formation and mineral deposition might happen and the material at the pre-existing fault can be altered therefore affecting the fault strength.

Since the Earth's crust is often critically stressed and involves pre-stressed faults of different sizes in many areas, it is challenging to foresee precisely the amount of seismicity that will be triggered. The exact locations of the faults and the precise current stress level of the area are difficult to determine and are often unknown. Figure 2.9 shows different physical mechanisms possibly causing induced seismicity.

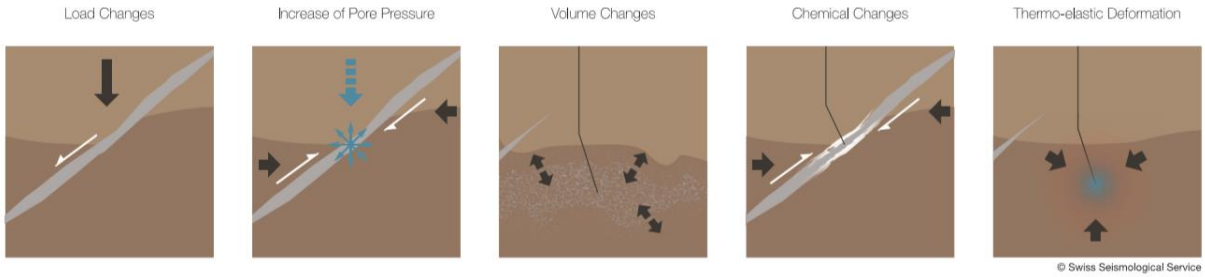

Figure 2.9 Different physical mechanisms for induced seismicity. Adapted from Hirschberg et. al. (2015).

2.9.2 Estimating maximum induced event size

There have been attempts to predict the magnitude of the induced events based on factors which can be reasonably well measured and controlled during the fluid injection.

One way to try to estimate magnitudes and probabilities of large events is a statistical method. Considering the Gutenberg-Richter distribution for natural earthquakes and using it with the induced events of the study area. One could try to estimate the possible magnitudes of the upcoming events based on magnitude-frequency trends of the observed seismicity and by calculating seismogenic index for the area as proposed in Van der Elst et al. (2016).

Other way of estimating the maximum expected magnitudes could be real-time monitoring of the seismic cloud caused by the induced seismic events and assuming that the maximum size of an event

is geometrically controlled by the size of the area disturbed by the fluid injection. This kind of approach was suggested in Shapiro (2011).

There also has been suggestion in McGarr (2014) that the maximum possible seismic moment for an induced seismic event would be related to the product of shear modulus of the medium and the injected fluid volume. In some cases the maximum magnitudes of the events were estimated somewhat correctly based on this quite simple principle. However there were also cases that did not follow the formula. For them the formula mostly overestimated the maximum magnitudes.

Different ways to predict the maximum magnitudes of the upcoming induced events can help to plan projects associated with induced seismicity safely both before and during the fluid injection.

2.10 PARAMETERS AFFECTING SEISMIC ENERGY RADIATION

2.10.1 Corner frequency

The seismic energy of an earthquake is not evenly radiated over the whole spectrum of its frequencies. It appears to be that there is a range of frequencies for which the ground displacement amplitudes are almost equal however, when the frequencies increase the equality in ground displacement amplitude ends at point called the corner frequency f_c after which, the displacement amplitudes will begin to decay drastically. Generally greater earthquakes have lower corner frequencies than smaller ones and so the spectral plateau gets smaller for them in comparison with the smaller ones. When considering the ground velocity amplitudes the greatest amplitude will be near the corner frequency where both the ground displacement amplitude and the frequency of the wavemotion are high. When considering unilateral faults with constant stress drops the f_c scales with the fault size. However in cases of bilateral faults there can be several corner frequencies. Figure 2.10 shows the behaviour of the source spectra considering measurable seismic moment and frequency.

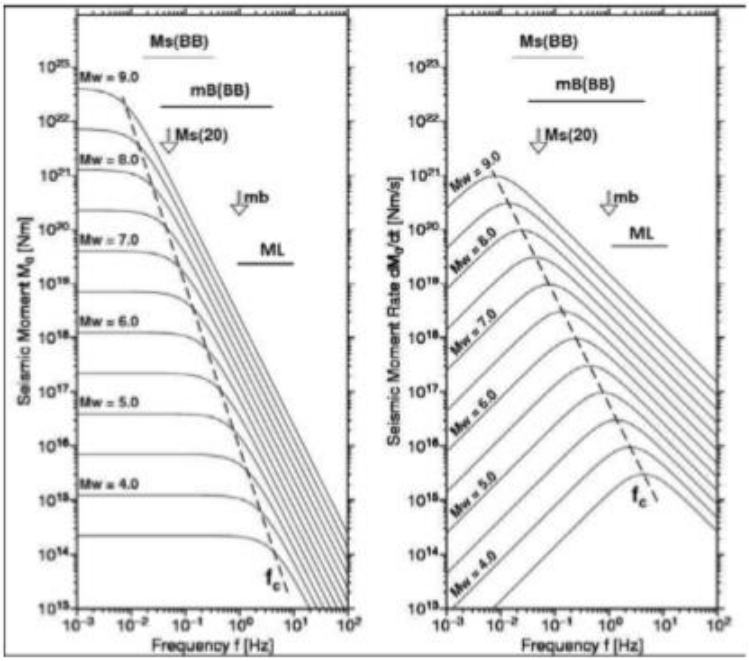

Figure 2.10 The corner frequency compared to the calculated seismic moment. On the left side is the source spectra of ground displacement amplitudes as function of frequency. The stress drop is constant for all cases. On the right side is the same data as in the left but for ground motion velocity amplitudes scaled to seismic moment rate. The maximum of the seismic energy is radiated around the corner frequency. Adapted from Bormann (2012).

Considering the things mentioned about corner frequency a seismometer used in recording nearby seismic event still having high frequency content should have high enough measurement interval in order to record the maximum amplitudes correctly at high frequencies. For more teleseismic cases lower measurement intervals can be enough. As a notice the peak ground velocity is good estimation for the damage potential of the earthquake since a higher ground velocity tied with high amplitudes seems to be more damaging than slower ground velocity with the same amplitude according to Bormann (2012).

2.10.2 Influence of rupture parameters

Rupture velocity and duration also play a role when considering how the seismic energy radiates from the source. The rupture formation affects how the energy radiates from the source during the rupture process and so it affects the length of the body wave trains on the seismogram. The rupture duration tends to increase with the magnitude, generally speaking. The rupture velocity is expected to be lower than the shear-wave velocity at the site, ranging usually between 0.2 and 0.9 times the velocity of the S-wave. Taking rupture parameters into account becomes more important for higher magnitude events when determining event magnitudes.

2.10.3 Factors affecting the seismic efficiency

The ratio between the radiated seismic energy as seismic waves and the seismic moment of the event appears to be related to the rupture model (how the rupture mechanically evolves), rupture

velocity and stress drop. Stress drop means the difference between the stress before and after the seismic event acting in the source region. The stress drop can be quite hard to estimate with great accuracy in the real world. According to Bormann (2012) higher stress drops are expected to lead to higher seismic efficiency (seismic efficiency expresses how much of the total energy released is released as seismic waves, with high seismic efficiency larger amount of the total energy is released as seismic waves compared to a case with lower seismic efficiency). The seismic efficiency appears not to stay constant between different event sizes and is affected by several factors as stated earlier.

The stress drops are expected to be reasonably close to each other for the induced seismic events in this study since they originate from the same area and are relatively close to each other in terms of magnitude.

2.11 Magnitude scales

It is desirable to have a way of expressing the size of an earthquake in a quantitative way. This is often done by using earthquake magnitudes. The first magnitude scale was introduced by Richter in 1935 to measure the size of an earthquake based on instrumental response. Nowadays there are many different magnitude scales used in seismology. In this section their theoretical basics will be discussed further with focus on the local magnitude scale, M_L. This focus is chosen since the magnitude scale used in this study is the Finnish local magnitude scale which is based on the Richter scale. Commonly the magnitude scale tries to correct the results for the epicentral distance and source depth of the event, whereas the intensity scale tends to quantify the local effects caused by the earthquake on the surface. The correction is needed because of the effect called geometrical spreading introduced in the section 2.3. Epicentral distance and the source depth together can be used to determine how far from the origin point the wave has travelled and therefore how much the amplitude has decreased because of the energy being divided into a spreading area. Magnitudes are often marked with letter M following a letter specifying the magnitude further. It is important to know which magnitude scale is used since they are defined differently even if they in many cases would give somewhat similar results. Different magnitude scales use different seismic wave types and different periods for amplitude measurement. Some scales also tend to saturate faster than others in case of large event sizes.

Generally there are few assumptions that the magnitude scales typically follow: larger seismic events produce higher amplitudes for a given source-receiver geometry. The logarithm of the amplitude is used since the relative variation can be very high between different events. The magnitudes also are proportionate to the seismic energy that is radiated from the source and thus are proportionate to the velocity of the ground motion. A magnitude scale typically takes into account the decay of the

ground motion with the epicentral distance and the source depth. The maximum ground motion value measured often offers the best and most stable estimate for the magnitude of the event and thus the size and energy released. A magnitude scale typically also involves a way to take regional effects into account. The effects might depend on regional crustal structure or the soil cover at the site and there can also be individual station corrections.

Generally the formula for magnitude scales that are based on ground displacement amplitude is:

$$\mathrm{M} = \log\left(\frac{A}{T}\right)_{max} + \sigma(\Delta, \mathrm{h}) + \mathrm{C_r} + \mathrm{C_s} \qquad (9)$$

where M is the magnitude, A is measured amplitude, T is period of the measured amplitude, $\sigma(\Delta, h)$ takes geometrical spreading into account, C_r is correction for regional effects and C_s is correction for station error.

There are also methods to determine earthquake magnitudes without the usage of direct amplitude records. A quantity called seismic moment can be calculated from the amplitude spectra produced by a seismic event. The theoretical basis of the method is that the seismic moment is directly related to the amount of "work" done by a seismic shear source, therefore being determined by the shear modulus of the material, average displacement after the rupture and the rupture area. The magnitude calculated using the seismic moment is called as the moment magnitude, often marked with M_W. Determining the magnitude using this method is more complicated but is less prone to error sources associated with traditional amplitude measurement. For the magnitude determination of this study the moment magnitudes will not be used but can be expressed for earthquakes mentioned in text.

2.11.1 The Richter magnitude scale

As said earlier in section 2.11 the first scale for magnitudes of seismic events was developed by Richter in the 1930s. This scale was specifically crafted for earthquakes in California in the United States. The scale was based on the observation that the logarithms of maximum ground motions decayed along parallel curves for many seismic events. The observations were made using Wood-Anderson torsion seismometers and the scale is originally meant to be used just with these particular instruments. The idea of the scale is that the scale expresses relative size of an events compared to a reference event.

This can be expressed as:

$$\mathrm{M_L} = \log(\mathrm{A}) - \log\,(\mathrm{A_0}) \qquad (10)$$

where A and A_0 are the displacement amplitudes of the event and the reference event at a prescribed distance. In the Richter scale the reference event was chosen to be event with $A_0 = 1 \times 10^{-3}$ m at an epicentral distance of 100km.

The reference event corresponds to $M_L 0$. With the usage of this event the equation (9) was written as:

$$\mathrm{M_L} = \log(\mathrm{A}) - 2.48 + 2.76\log\,(\Delta) \qquad (11)$$

The application of the original Richter scale is restricted by several factors: it only works with certain instrument which has natural period of 0.8 s and static magnification of 2800 and it is based on shallow, mostly less than 15km deep seismicity of the area of southern California. The simple facts that nowadays the standard Wood-Anderson-instruments are not used anymore and that most earthquakes do not happen in southern California somewhat reduce the application of the scale globally. The scale however has worked as a basis for many other local magnitude scales specific for certain regions. If considering engineering applications, it can be mentioned that many structures have their natural period reasonably close to 0.8 s so the extent of earthquake damage can be related to M_L surprisingly well.

2.11.2 Finnish local magnitude scale

The Finnish local magnitude scale was introduced in Uski (1996), where the magnitude formulas considering the area of Finland in the Fennoscandian shield are derived based on the principles of the Richter scale and synthesized Wood-Anderson recordings from local and regional earthquakes. In total 1259 recordings from 216 earthquakes were used in establishing the magnitude scale. Hypocentral distance range was from 25 km to 1940 km and reported magnitudes varied from $M_L 1$ to $M_L 4$. The earthquake data used was from February 1979 to June 1994. The main method for determining constants for the terms involved in the magnitude scale was the application of regression analysis. The procedure will be explained further later in this section.

In most basic form a local magnitude scale formula can be written as:

$$\mathrm{M_L} = \log(\mathrm{A}) - \log(\mathrm{A_0}) + \mathrm{S} \qquad (12)$$

where A is measured amplitude, A_0 is the reference amplitude and S is station correction. The definition is quite simple and arbitrary but it is still used as basis for many local and regional magnitude scales. Often the local and regional magnitude scales are calibrated to be in agreement with the Richter scale. The reason behind why local magnitude scales are used instead of seismic moment even if they only approximately estimate the total energy released by an earthquake is that they are fairly simple to calculate and use in daily seismic analysis.

Before the Finnish local magnitude scale the local and regional earthquakes in Finland and Sweden were calculated mostly by using M_L(UPP) provided in Wahlström (1979) and Wahlström and Ahjos (1982). M_L(UPP) is a local magnitude scale established for Fennoscandian area, the abbreviation "UPP" origins from the Uppsala University.

The scale however was instrument dependent and designed for certain short-period seismograph stations.

When establishing the Finnish local magnitude scale the amplitudes and periods which would have been read by the WA-instruments were synthesized by converting the short-period vertical records into synthetic WA-seismograms. The reference value (-log A_0) was derived from maximum amplitudes and periods of these synthetic signals.

The synthetization of the Wood-Anderson records was done by deconvolving the network seismograms with the station system response and after that the ground displacement was convolved with the response of the standard Wood-Anderson-instrument. Actions were made to minimize the amplification of noise in the process. In the synthesis Wood-Anderson-instrument damping ratio 0.8 and gain 2800 were used as theoretical values. The maximum peak-to-peak amplitudes used were measured from Sg and Lg phases. Generally in Fennoscandia the largest arrival belongs to these phases. In 1956 Richter stated that the amplitude should be measured from the largest peak of the S-wave train when determining the magnitude.

The majority of the events used to establish the Finnish local magnitude scale was located in the coast of western Norway or along the coast of Bothnian bay. Most of the data was associated with relatively large distances (90% between 400 km and 1200 km). It should be mentioned that since southeastern part of Finland is naturally practically aseismic quite few observations with distances

less than 100km were available. Also the azimuthal coverage could have been better since more than 90% of the events had all used stations located in just one azimuth quadrant.

Originally Richter instructed to measure amplitudes as mean of two horizontal component peak values, but in the establishing of the Finnish M_L scale the amplitudes were measured from the vertical component. In order to correct this the formula was determined so that the difference between vertical and horizontal Sg/Lg phase amplitudes is compensated. The ratio between the horizontal and vertical shear-wave amplitudes was determined and it appeared be dependent on the hypocentral distance according to log(H/Z) = 0.00009R, where H is the amplitude of horizontal component, Z is the amplitude of vertical component and R is the hypocentral distance. This term is integrated into the final magnitude formula.

When calculating the -log A_0 for Fennoscandia this correction function was separated into two parts: one to consider the geometrical spreading and one to consider the anelastic attenuation. This can be expressed as:

$$-\log(A_0) = \alpha \log(R) + \log(e)\,\gamma R \qquad (13)$$

where α is the geometrical spreading coefficient, γ is frequency independent anelastic attenuation factor, e is the Euler's number and R is the hypocentral distance. When assuming the anelastic attenuation as frequency dependent the gamma becomes $\gamma_0 f^n$, where f is the frequency associated with the amplitude and n is a constant.

The regression described next was conducted by using linear least squares method, attempting to minimize the sum of the squared residuals of the calculated magnitudes for the function by adjusting the used parameters for the correction terms.

For the regression to bilinear form the linear regression equations used were:

$$\log(A_{ij}) + C = \alpha_1 \log(R_{ij}) - \Gamma f_{ij}^n R_{ij} + M_i - S_j + e_{ij} \qquad \text{for } R \le R_1 \qquad (14)$$

and

$$\log(A_{ij}) + C = \alpha_1 \log(R_1) - \alpha_2 \log(R_{ij}/R_1) - \Gamma f_{ij}^n R_{ij} + M_i - S_j + e_{ij} \quad \text{for } R > R_1 \qquad (15)$$

where C is constant that anchors the function to -logA_0(HB), M_i is the regressed magnitude for the earthquake i (i = 1, …, 216), Γ is the anelastic attenuation coefficient (log(e)γ_0) and e_{ij} is error following normal distribution with zero mean. S_j is stations correction for station j. R_1 is the transition distance from Sg type to Lg type geometrical decay.

Later it was tested if the -log(A_0) function could be modelled using only function (14) for the whole distance range. The regression to linear form was performed succesfully and following values for the parameters were received:

For α values of 1.27±0.06, 0.83 (fixed value) and 1.42±0.07 were received, depending on distance. For γ 0.41±0.04 and 0.08±0.08, depending on distance, for n 0.36 (fixed value).

Since the region of Fennoscandia differs from the California geologically, the attenuation properties are also clearly different. In Richter's formula -log(A_0) has value of 3.0 at distance of 100 km.

For the reasons of requirement of near-source calibration and sufficient amplitude control a distance of 60 km was chosen as the reference distance in Uski (1996). The -log(A_0) was adjusted to be 2.678 at 60 km according to -log(A_0)(HB). The -log(A_0)(HB) is a revised -log(A_0) for southern California based on more modern regression methods and a larger database than the original -log(A_0) determined by Richter. The abbreviation "HB" origins from the names of the authors in Hutton and Boore (1987) where the term was determined. The predominant Sg-wave frequency considering displacement at the calibration distance of 60 km was 10Hz in the database used in Uski (1996).

The results for various distances were:

$$M_L(f) = \log(A) + 1.27\log(R) + (0.00009 + 0.00041f^{0.36})R + 0.363 + S \qquad (16)$$

for distances $R \leq 350$ km. A is the measured zero-to-peak WA-amplitude in mm, R is the hypocentral distance, f is the frequency and S is the station correction.

$$M_L(f) = \log(A) + 0.83\log(R) + (0.00009 + 0.00041f^{0.36})R + 1.482 + S \qquad (17)$$

for distances 350 km ≤ R ≤ 1900 km

$$M_L = \log(A) + 1.42\log(R) + 0.00017R + 0.148 + S \quad (18)$$

for distances R ≤ 1900 km.

The correction between using vertical (Z) component shear wave amplitude instead of horizontal (H) component was found to be dependent on distance according to log(H/Z) = 0.00009 R. The correction is involved in formulas (16-18).

2.11.3 Currently in use magnitude formula

Currently in the Institute of Seismology of the University of Helsinki (later in this text ISUH) following formula is used in daily analysis (Finnish local magnitude scale is often written as M_L(HEL) in records, the abbreviation "HEL" origins from University of Helsinki):

$$M_L(HEL) = \log(A) + 1.42\log(R) + 0.00017R + 0.148 + S \quad (19)$$

where R is the hypocentral distance (km), S is station correction (but in practice it's quite small), A = synthesized Wood-Anderson trace amplitude (half the peak-to-peak in mm) measured from the vertical component seismogram.

Since the data processed in analysis is provided in nanometers and considers ground motion instead of WA-instrument response a modification is used with the formula in order to approximate the would be response from the WA-instrument.

The modification can be written as follows:

$$\log(A) = 0.86\log(a) - 2.34 \quad (20)$$

where a is the ground motion amplitude (half the peak-to-peak amplitude in nm measured from Sg/Lg wave maximum on original "unfiltered" seismograms)

This kind of approximation removes the need for "synthesizing" WA-instrument responses and the observed ground motion data can be used directly. A similar approximation for WA-response is shown in Alsaker (1991), since the computation of synthesized WA-amplitudes is quite time consuming in routine seismological analysis.

In the paper Alsaker arrived at formula

$$\log(A)_{WA} = 0.925(\pm 0.014) \cdot \log(A_{obs}) - 2.32(\pm 0.03) \quad (21)$$

where A_{obs} corresponds to the $\log(\mathrm{a})$ in formula (20). This was calculated using maximum likelihood regression analysis between synthesized WA-amplitudes and amplitudes measured from raw (observed) seismograms corrected for system response.

The frequency independent formula for the M_L (HEL) scale now becomes:

$$M_L(HEL) = 0.86\log(a) + 1.42\log(R) + 0.00017R - 2.19 + S \quad (22)$$

During the Fennovoima project in 2010-2013 ISUH noticed that the magnitude scale does not apply well for near-source data, i.e. those recordings within 100-150 km from the source. Additional distance correction was derived for distances less than 150 km and it has been in test use since then.

If R < 150km $$\mathrm{M_L(HEL)} = \mathrm{M_L(HEL)} + 0.53 - 0.003\mathrm{R} \quad (23)$$

For the cases where R is less than 150 km (almost all of them) formula (22) with addition of (23) will be used in magnitude calculation of this study considering the induced seismic events.

With addition of this modification attempting to correct the underestimation of the magnitude values for near-source amplitude records, the complete magnitude formula for M_L(HEL) becomes:

$$M_L(HEL) = 0.86\log(a) + 1.42\log(R) + 0.00283R - 1.66 + S \quad (24)$$

The formula's suitableness will be assessed in this study. The currently used formula for Finnish local magnitude scale in daily analysis does not involve frequency component.

2.11.4 Possible problems arising from the M_L(HEL) scale with near-source events

It is noted in Uski (1996) that during the determination of the M_L(HEL) scale there was no usable earthquake data from less than 25 km distances and data even from less than 100 km distances was quite scarce as noted before in this chapter. It is also noted that the results of Grad and Luosto (1994) indicate that the amplitude decay in the study area may be much higher at distances of roughly 20 km compared to distance range from 20 km to 120 km. This assumption most likely origins from the local variations in the layers of the uppermost parts of the crust and how the higher velocity layers in the Fennoscandian crust are located according to Grad and Luosto (1994). The attenuation function of the M_L(HEL) scale might therefore be less trustworthy at near-source distances.

2.12 EARTHQUAKE LOCATION DETERMINATION

When dealing with earthquake data it is generally useful to know when and where the event has taken place. The knowledge is also required for the magnitude calculations, since as mentioned earlier in this chapter the epicentral distance and the source depth must be known in order to take the geometrical spreading into account. The time of the event is called as origin time and the location as the hypocenter. The hypocenter determines the event's location in x, y and z whereas the epicenter is point on Earth's surface above the hypocenter. When locating earthquakes, its often easiest to treat them as point sources. In reality the approximation is more valid for smaller events than large events with possibly tens or hundreds of kilometers of rupture. The hypocenter though can still be resolved even in cases of large ruptures since the rupture velocity is less than the velocity of the emitted P-wave regardless of the rupture size or the event duration.

The theoretical basis of one often used method for earthquake location is provided in Shearer (1999). In the method the origin time alongside the hypocenter can be described with four parameters: T, x, y and z.

We refer to the mentioned parameters as model and define a model vector:

$$m = (m_1, m_2, m_3, m_4) = (T, x, y, z) \qquad (25)$$

Next let's suppose that n observations considering the travel times (t_i) are known at individual seismic stations. These observations can be used to invert the m parameters.

For this a reference Earth model is required. Now for values of m expected travel times can be calculated.

$$t_i^p = F_i(m) \tag{26}$$

where F is operator which gives the estimated travel time for each station and t^p stands for predicted travel time.

The difference between observed and estimated times can be written as:

$$r_i = t_i - t_i^p = t_i - F_i(m) \tag{27}$$

where r gives the residuals for each station. The objective is now to find the m which gives overall the smallest possible residuals between estimated travel times and the observed ones. In the simplest 1-D Earth model the calculations are fairly simple but when considering models with more dimensions and more complicated velocity models the computation becomes much more demanding.

The different velocities of seismic phases are often used when determining the event location. For example, P- and S-wave arrivals can be used to directly estimate the source-receiver range at the station. For this purpose, both P and S arrivals were picked for the datasets used in this study.

Generally it can be said that the location is much more reliable when the event takes place inside the seismic station network when comparing to case where it takes place outside it. For determining the depth of the event, it is useful to have station near the event hypocenter. Luckily in the case of the events of this study the events happen inside the network and many near stations are usable. However unknown faults and errors in velocity model may affect the end results.

Often the situation is that the error in the location is dominated by the effects of the unknown 3-D (therefore unmodelled) velocity structure. This affects mostly the absolute locations estimates though relative locations between events are much easier to achieve. This is because the local lateral variations in the velocity structure have nearly the same effect on the recording from more distant stations for all the events.

According to Shearer (1999) instead of directly searching for minimum origin parameters all over the possible solutions it is often computationally more feasible to use a less direct approach.

A standard technique used is to linearize the problem by using:

$$m = m_0 + \Delta \mathrm{m} \tag{28}$$

where m_0 is the currently guessed location as the best candidate and m is the new guess within a small distance from the initial guess. Then the predicted times can be approximated using a Taylor series.

This way $\Delta \mathrm{m}$ can be found for which the residuals are minimized. The best fit can be obtained using the standard least squares method. The process is repeated iteration by iteration after the location converges. The method works reasonably fast when the initial m_0 is not very distant from the true location.

According to Lay (1999) as initial guess for a local seismic event the difference between the P- and S-wave velocities can be used alongside the Wadati diagram method to determine the origin time of the event. The diagram consists of S-P-wave time difference as the y-axis and P-arrival time as the x-axis. Station records are plotted and form a line which's intercept point with the x-axis gives the origin time. The slope of this line is related to Poisson's ratio. For the next step when the P-wave velocity is known (average v_P is estimated as well as possible) the rough event location can be obtained by triangulation. The Epicenter should be where the travel distance circles intercept. For this at least 3 stations are needed, one station for each unknown parameter. The focal depth can also be determined from this by taking square root of the differences between the squares of the calculated propagation distances and the distances along the surface to the epicenter. The whole method is called the method of circles.

2.13 PAIKKA-PROGRAM METHODS FOR EARTHQUAKE LOCATION DETERMINATION

The Paikka-program calculates the earthquake hypocenters based on the picked P- and S-wave arrivals by using a standard linear least-squares algorithm. The crustal velocity model used by the program is one-dimensional and consists of layers with constant seismic wave velocity. For the uppermost 15 km thick layer inside which the expected first arrivals travel through the velocities for P- and S-waves are 6200 m/s and 3620 m/s. The same velocity model is used in the daily analysis in ISUH.

3 FENNOSCANDIAN SHIELD AND ITS MAIN GEOLOGICAL FEATURES

The Fennoscandian shield is a shield area situated in the north-western part of the East European Craton. As a total the shield is most sizable area considering exposed Precambrian rock in Europe (Lahtinen 2012). Large parts of Finland's area constitute to the Fennoscandian shield, but as total it includes large parts of Sweden, Norway and North-western Russia. The oldest rocks contributing to the shield are from the Archean period (>2500 Ma) and in some locations of the north-western part of the shield the ages of the rocks may reach 3000 Ma. When moving into south-western direction from the north-eastern corner of the shield the rocks generally get younger, but the ages are still considerably old. Much of the rock mass is from the Paleoproterozoic (1600-2500 Ma) or Mesoproterozoic eras (1000-1600 Ma). Phanerozoic or younger rock is more uncommon as can be observed from the Figure 3.1.

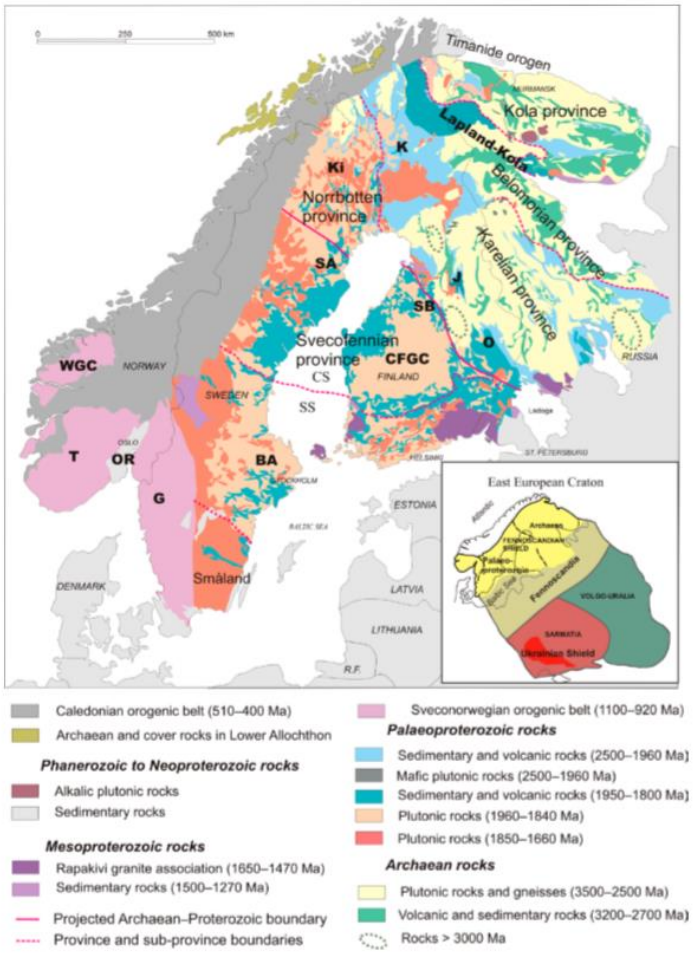

Figure 3.1 Main geological features of Fennoscandian shield. Colours corresponding to rock types of different geological periods are listed in the legend. As a general notice the oldest rock are found in the north-eastern parts whereas youngest rocks tend to be found in the south-western parts of the shield. Adapted from Lahtinen (2012).

3.1 SOUTHERN FINLAND AREA

When considering tectonic provinces of Finland, the southern part can be named as Southern Finland Subprovince, which is a part of the Svecofennian tectonic province. Finland's division to different geological provinces is shown in the Figure 3.2. The geological era to which the rocks in the Southern Finland Subprovince generally belong to is the Paleoproterozoic era. As with most of the Fennoscandia the area has enjoyed reasonably rich geologic history. According to Nironen (2017) diverse geological suites and lithodemes have been found when studying the area. There exists many different structures that have been formed in volcanic, plutonic, intrusic and at some point metamorphic processes. The formations and structures however are not going to be discussed individually in more precise manner since they provide almost no further useful information at this point considering the aim of the study.

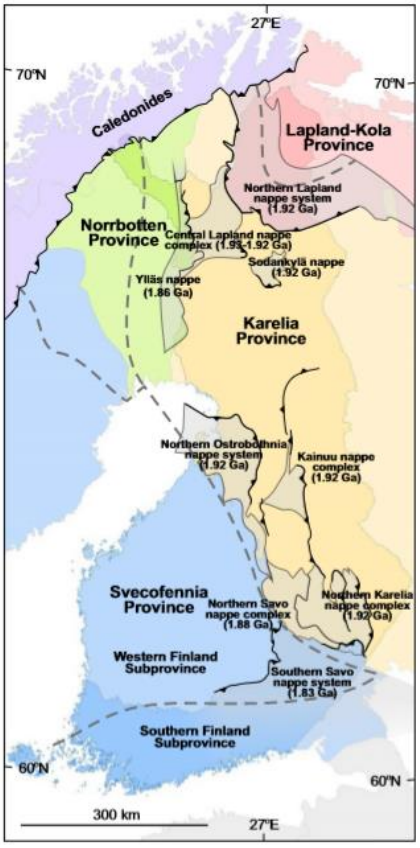

Figure 3.2 Geological provinces of Finland. Southern Finland Sub province where the study area is located can be seen marked in the map. Adapted from Nironen (2017).

3.2 GEOLOGY AROUND THE ST1 DRILL SITE

Considering the geological history of the study area the basement rock is from Precambrian period. According to Kwiatek (2019) the Svecofennian basement rock is covered in 20 m or less thick layer of quaternary glacial deposits and clay-rich soils. The basement rock has experienced folding, foliation, jointing and faulting during late Mesozoic plate motions and glacial rebound during the Holocene

period. The rock types encountered in the basement rock are deformed metamorphic and intrusive granites, pegmatites, quartzo-feldsparic gneisses and amphibolites. Figures 3.3 and 3.4 illustrate the thickness of the soil layer and rock types of the study area.

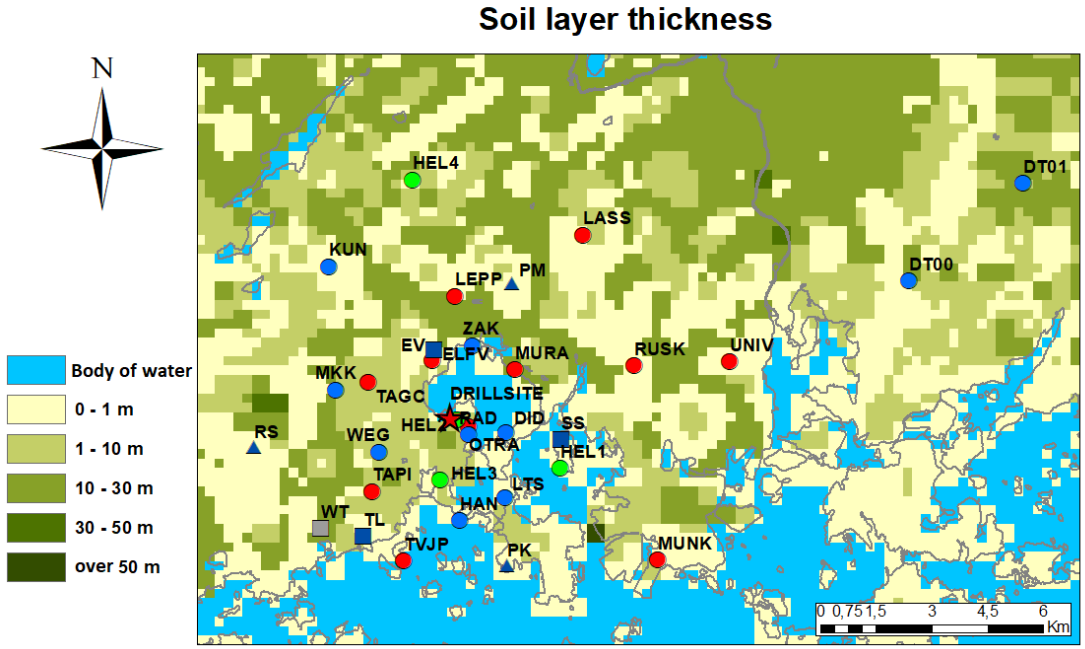

Figure 3.3 Soil layer thickness in the Espoo/Helsinki area. The drill site is marked with the red star on the map and the stations of the seismic network are illustrated on the map. Different subtypes of seismic station are marked with their own symbols. The data illustrated in this map was provided by The Geological Survey of Finland (GTK) Hakku service.

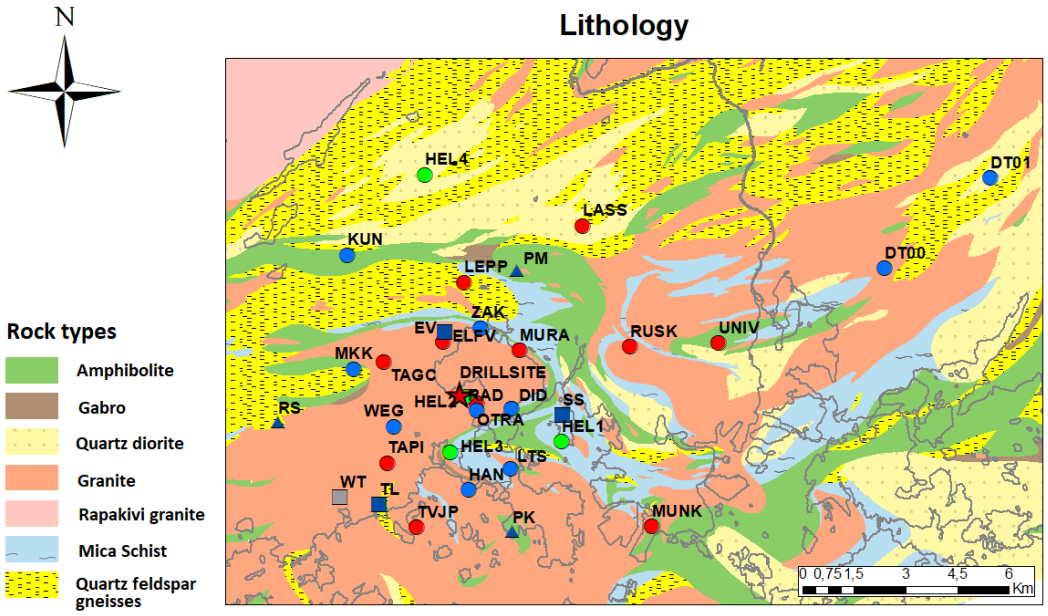

Figure 3.4 Rock types in the Espoo/Helsinki area. The drill site is marked with the red star on the map and the stations of the seismic network are illustrated on the map. Different subtypes of seismic station are marked with their own symbols. The data illustrated in this map was provided by The Geological Survey of Finland (GTK) Hakku service.

It can be concluded that most of the rock is igneous or metavolcanic based on figure 3.4. A rather high amount of the igneous rock is granitic in composition.

There are a few faults located in proximity to the drill site. According to Elminen (2008) a fault zone called Porkkala-Mäntsälä fault zone is located roughly less than 10 kilometers to the northwest from the drill site. It is assumed to be roughly 50km in length and is oriented in NE-SW direction. In addition to that there exists another reasonably long N-S oriented fault called Vuosaari-Korso fault going through the Helsinki area, but it is much further from the drill site. In Elminen (2008) both of these faults are classified as ductile reverse faults. These two are the only major faults located somewhat near the drill site. Also roughly 1.5 kilometers to south-east from the drill site lies a supposedly inactive SE dipping thrust fault but it is much smaller than the earlier mentioned major faults. In addition to this there exists several smaller faults and shear zones in the Espoo/Helsinki area. The faults and shear zones are illustrated in Figure 3.5.

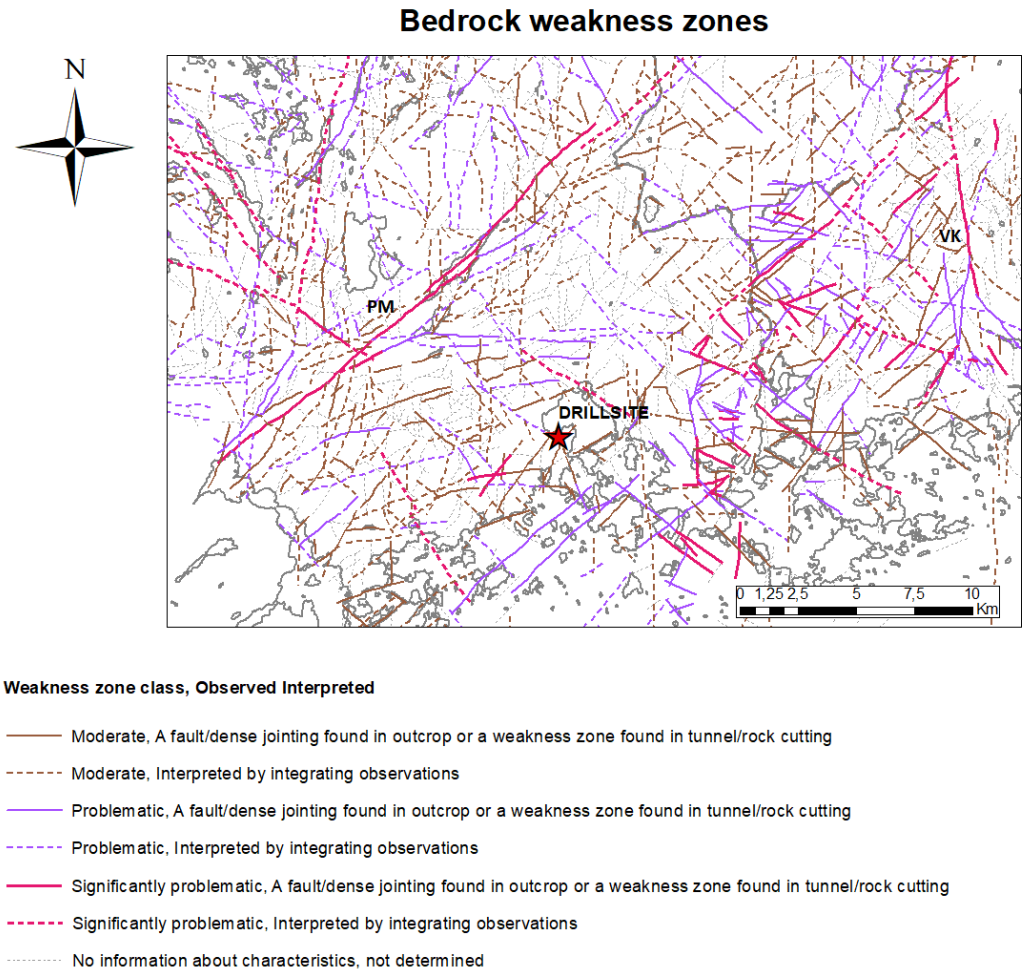

Figure 3.5 Faults and shear zones located in the Espoo/Helsinki area. markings for weakness zone types are marked in the legend. The drill site is marked with the red star on the map. PM corresponds to Pirkkala-Mäntsälä fault and VK corresponds to Vuosaari-Korso fault. The data illustrated in this map was provided by The Geological Survey of Finland (GTK) Hakku service.

According to Kwiatek (2019) the drill bit seismic data would suggest the existence of an additional south-east to south-west 70 to 80 degrees dipping structure. The structure is supposedly located just 1-2 kilometers north-west from the drill site and could possibly intersect the well at depths of 5.4 km to 6.2 km.

Considering the seismicity there has been in total three natural seismic events near the drill site according to data from ISUH. The one with the highest magnitude (M_w 2.6) took place on 2011 in the Mäntsälä fault. Though the hypocenter of the event was quite far from the part of the fault which is nearest to the drill site. In addition to that 2 events of magnitudes M_w 1.7 and M_w 1.4 took place in Laajalahti area in Espoo in 2013. These three events are the only instrumentally registered natural earthquakes in the Helsinki area in recent history so it could be said that the area has very low background seismicity.

According to Kwiatek (2019) the stress magnitudes at 6.1 km depth are estimated to be S_H^{max} = 240 MPa, S_H^{min} = 110 MPa and S_V = 180 MPa. Maximum horizontal stress direction in the drill site area is N110°E. The pore pressures at the 6.1 km depth are assumed to be hydrostatic and roughly 60 MPa. If a friction coefficient of 0.6 is assumed it is mentioned to make it in theory possible for an optimally oriented fault or fracture to be reactivated by moderate fluid pressure increase.

3.3 NATURAL SEISMICITY

Finland's area in the Fennoscandian shield is situated in a stable continental region and experiences relatively low amount of natural seismicity. Generally the earthquakes occurring in the Fennoscandian area are located in the uppermost part of the crust, at less than 15 km depths. Clear minority of the events happen in the middle or lower crust at 16 km to 45 km depth range (Kortström et. al. 2018). Most common focal mechanisms are combinations of strike-slip and reverse faulting. The natural seismicity of the area in commonly related to intraplate and plate margin processes (there are no plate margins in direct vicinity of Fennoscandia, but the opening of the North Atlantic Ocean affects the stress state of the area). Causes for the seismicity are postglacial rebound, stress caused by opening of the North Atlantic Ocean and local stress originating from gravitational or compositional variations in the crust. There are some areas which are seismically more active in the Fennoscandian shield often associated with postglacial fault zones or zones otherwise affected by crustal weakness caused by shear zones and faults. There has also been shallow earthquake swarms associated with the Rapakivi granite batholith in the Wiborg area. The

Helsinki and Espoo area is however not associated by any of these features causing higher intraplate seismicity. (Korja et. al. 2015)

4 GEOTHERMAL ENERGY SYSTEMS

Characterization and planning of different types of geothermal energy systems is discussed in reasonable extent in the "Good Practice" Guide for Managing Induced Seismicity in Deep Geothermal Energy Projects in Switzerland published by Swiss Seismological Service in 2017 and in Hirsch (2015). Based on the characterization the geothermal projects can be divided into two different classes: "near-surface"- and "deep geothermal projects". The near-surface projects involve for example groundwater heat pumps and ground-coupled heat exchangers. They often involve closed systems where no fluid is exchanged with the surrounding material. These types of systems have not been observed to cause induced seismic activity. As a rule of a thumb it can be said that projects expanding to depths of roughly over 400-500m can be considered as deep geothermal projects. Considering the depth (6.1 km) of the ST1 drillhole it clearly belongs to the latter category.

When considering the deep geothermal projects they can be subdivided further based on the temperatures involved and the exploitation type. High-enthalpy reservoirs are often used worldwide for electricity production. The high temperature requirement however puts constraints for the location of these type of projects and they are often used in vicinity of volcanic areas. For this type of projects the temperatures in the underground can be even few hundred degrees Celsius. The low-enthalpy reservoir involving projects can be subdivided into three more subtypes: deep borehole heat exchangers (the ST1 project considered in this study corresponds to this category), hydrothermal- and petrothermal heat exchangers. In the low temperature systems the temperatures can be as low as just above 100 degrees, which can't be used for electricity production efficiently, but instead for district heating. This however allows them to be placed less strictly and they do not require so special geological conditions.

In petrothermal and deep borehole heat exchangers the target reservoir involves rock formations with low permeability which require some enhancement to be done before the desired flow rates can be achieved. Because of this these types of projects are called as EGS, Enhanced Geothermal system. The hydrothermal projects are not considered as EGS since they often target already permeable, often sedimentary rock formations where the required fluid flow is possible in their natural state. Figure 4.1 shows different types of systems exploiting the temperature conditions of the subsurface.

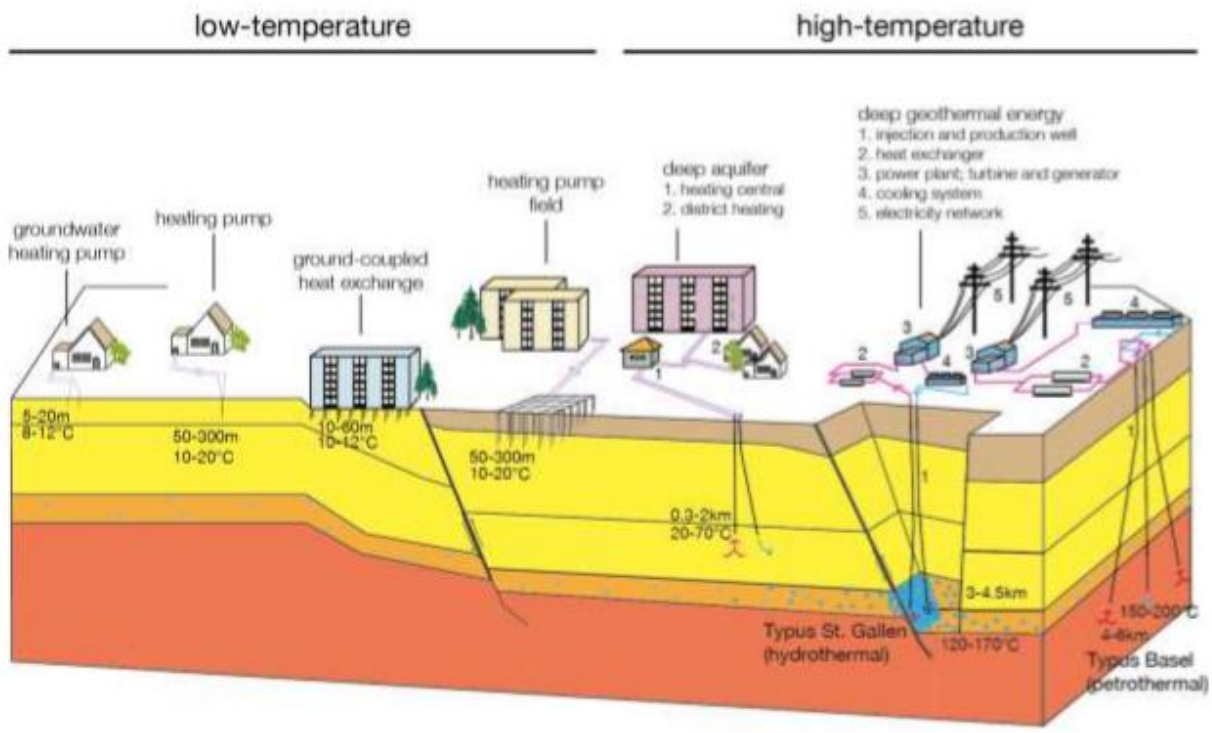

Figure 4.1 Different types of geothermal energy systems. The division between the low-temperature and high-temperature systems is clearly illustrated in the figure. the approximate required depths for each system are marked in the figure alongside the target temperatures. Adapted from Hirschberg (2015).

There are several reasons why the deep geothermal energy systems are quite challenging projects. They also are a reasonably new technology so the experience with them at this point is quite limited when comparing it to more established types of technologies involving drilling such as oil and gas production. Since the reasonably limited experience and amount of earlier projects there is not too much of scientific data available considering them. Because they are known to be related with induced seismic activity they can easily receive negative public attention.

When considering the deep geothermal energy projects the fact that they can be placed in many kinds of different geological areas gives them the change to be placed near residential zones when they are used for district heating purposes. And even if they were used for electricity production the local heat use would increase the profitability of the project. However their location near urban areas also increases the dangers of the induced seismic activity they might cause because of the building and population density compared to a EGS that would be located in a more rural area.

When creating the enhanced reservoir, the induced earthquakes are a direct consequence of creating the system. In order to achieve the desired heat output and therefore for the project to be economically viable the induced events will and must be caused. Balancing the economic aspects and the dangers is very much needed, but there is still reasonably low amount of experience related to enhancing of the system and the induced seismicity.

If the deep geothermal project would be hydrothermal the location could be near a fault zone because of the increased permeability. Though in Wiemer (2017) is mentioned that these types of projects can prove to be more seismogenic than expected. However this risk is not related to ST1 project since the project is not hydrothermal and therefore requires not to be located near a fault zone.

4.1 SEISMIC RISK GOVERNANCE AND THE TRAFFIC LIGHT SYSTEM

Wiemer (2017) offers many suggestions for risk management considering EGS projects. It is desirable to reduce the risks caused by such projects in order to make them economically viable. Different types of risk assessment are required in different project phases. Since this study is focusing on the induced seismic activity caused by ongoing project for the time when the fluid pumping is being done, the chapter will be more focused on the measures that need to be taken in this phase of the project although risk assessment procedures for other phases will be also mentioned shortly.

According to the Wiemer (2017) the geothermal projects can be divided into 4 different categories based on the expected risks involved with the project: category 0-, 1-, 2- and 3 projects. The risk management required increases with the rank meaning that the category 3 projects require the most risk analysis and management. The ST1 project considered in this study corresponds to the category 3 therefore requiring the most severe measures in order to be considered well planned, economical and safe. The requirements and required risk management for the categories 0, 1 and 2 will not be discussed further.

4.2 CATEGORY 3 PROJECTS

Projects belonging into the category 3 are typically petrothermal projects meaning that the permeability of the system has been increased. Typically they are located in basement rocks and have depths of over several kilometers. Projects of this category can also be located near fault systems or great amount of reservoir enhancing and stimulation is planned to be done. In this type of systems induced seismicity will certainly be experienced and it is also likely to result in felt events in residential areas near the system. As said in Wiemer (2017) category 3 events require “substantial risk assessment, monitoring, mitigation and public engagement”.

Since the study considers events occurring during the stimulation phase of the ST1 project we will next focus on the hazard and risk assessment that should be made during the stimulation phase for category 3 projects. Hazard and risk assessment during the planning phase of such a project will not be discussed in more detail.

4.3 HAZARD AND RISK ASSESSMENT RECOMMENDATIONS FOR STIMULATION PHASE OF CATEGORY 3 PROJECT

During the stimulation phase the forecasting models and assumptions considering the induced seismicity that have been made during the planning of the project should be validated and for example injectivity tests could be made for calibrating the assumptions made earlier about the induced seismic activity and ground motion. This can provide additional constraint to the forecasting models considering the seismic activity and its spatial distribution. Predictions and assumptions about the induced activity should be compared to the new observations and it should be tried to ensure that the operation happens within acceptable limits. There should be a clear mechanism how the hazard assessment considers the new data received during the drilling and stimulation of the reservoir. It is mentioned in Wiemer (2017) that a good way for doing this would be to take a phase-wise approach which is based on small steps of progress each followed by fast re-assessment of the seismic hazard and risks. It is important that the seismic monitoring is active and fully operational during the stimulation. The monitoring should happen in real time and there should be a so called ”traffic light system” (TLS) active during that time. The TLS system will be discussed further in the next section. Also it would be beneficial to offer predictions and information of the induced seismic activity in a transparent way to the general public in the affected area.

4.4 TRAFFIC LIGHT SYSTEM FOR EGS PROJECT

Suggestions about a traffic light system have been gathered in Wiemer (2017). The TLS is a risk reduction strategy that can be used during an EGS project to reduce the risks caused by the induced seismic activity. The TLS is designed to intervene when the induced seismicity and its risks are rising to unacceptable levels. In this case the operation must be either modified or stopped.

For creating a traffic light system for monitoring induced seismicity the very basis is to determine certain thresholds above which the operation is no longer acceptable. For an example a certain magnitude threshold can be placed which triggers certain colour of the traffic lights. If simply following the Gutenberg-Richter law there is roughly 10 times more events of magnitude M-1 than events of magnitude M. If this kind of relation is assumed it can be considered for example is a 1% chance for event of magnitude of M+2 acceptable if a event of magnitude M has been observed.

Since the economic success of the project involving permeability enhancing of a reservoir depends on the traffic light system it must be balanced between the economic factors and the public safety.

A traffic light system basically involves three colours: red/orange (meaning that the operation must be stopped or a “bleed-off” must be initiated meaning that fluids will be actively released from the borehole), yellow (operation can be continued but it can no longer be increased) and green

(operation can be carried on as planned). After an alert there is planned procedures and rules made for the resuming or restarting of the operation. Modification of the injection rate for example by using the traffic light system can be an effective way of risk reduction and a tool to control the amount of induced seismic activity. Though the reduction of the seismicity might not happen instantly when stopping or reducing the actions made for enhancing the reservoir.

The traffic light system can also involve other components than just the observed local magnitudes and the number of events of certain magnitude. Peak ground velocities or public response can also be considered when creating the system.

4.5 EGS PROJECTS WORLDWIDE IN SIMILAR GEOLOGICAL SETTINGS

Since the ST1 project takes place in crystalline bedrock and at roughly 6 km depths in an intraplate tectonic setting a few projects sharing roughly the same features will be summarized briefly.

4.5.1 Basel EGS project, Switzerland

The project is described in Häring (2008). In north-western Switzerland at the south-eastern margin of the Upper Rhine Graben a deep heat mining project was conducted in order to create an enhanced geothermal reservoir to be used in heat and electricity production during the year 2006. The geothermal plant was located near the city of Basel and the well utilized was supposed to be 5 km deep. The drill hole Basel 1 consisted of penetrating 2.4km of sedimentary rocks and 2.6km of granitic basement. The project involved extensive testing and planning alongside microseismic monitoring array and a traffic light system. The stimulation period was supposed to last 21 days in total during which the granite at the bottom of the hole would be hydraulically stimulated in order to achieve higher permeability.

The project resulted in extensive microseismic activity and the injection was decided to be stopped after just 6 days of stimulation after experiencing event magnitudes up to M_L 2.6. The planned procedures for this type of induced seismic behaviour were followed by stopping the stimulation and preparing to ”bleed off” the well to hydrostatic conditions. However in just 5 hours after the stopping of operation an event of M_L 3.4 took place. After the event during following 56 days three more events higher than M_L 3.0 were observed. Following these observations the project was suspended.

When comparing the Basel project to the ST1 project the most notable difference in the seismicity of the areas is that the Upper Rhine Graben at the Basel region has more features such as faults and rifts that indicate crustal weakness. Also the Upper Rhine Graben is seismically somewhat active experiencing minor seismic events frequently and occasional destructive events. Also the largest known historical earthquake took place in Basel in 1356 according to Giardini et. al. (2004) with

magnitude of M_L6.5-6.9. Another difference is that the temperature at 5km in Basel well was estimated to be as high as 190 degrees Celsius. Similarities between the two projects involve the depth range of the wells and the enhancement of the reservoir permeability in the crystalline rock basement.

4.5.2 Soultz-sous-Forets EGS project, France

The Soultz-sous-Forets project is described in Hooijkaas et al. (2006) and Gaucher et. al. (2015). The planning of the Soultz project started as early as 1984 in cooperation with the French BGRM (Bureau de Recherches Géologiques et Minières, the French Geological Survey) and German Geological Survey of Baden-Wurttemberg by mapping geothermal resources within the Upper Rhine Graben. The drilling and scientific activities associated with the project started in 1987 in Alsace, France. During next 10 years two boreholes GPK1 and GPK2 were drilled to approximately 3-3.5 km depth and a series of different hydraulic, geophysical and geological investigations. In the area the rock becomes granitic after penetrating sedimentary layer with a thickness of 1.5 km. In the end of 1997 experimental work was started in order to develop an EGS for the purposes of electricity production. The borehole GPK2 was deepened up to 5 km depth and later a new borehole GPK3 was drilled in its vicinity to roughly the same depths. At the start of the 21st century a fourth borehole GPK4 was drilled also extending to approximately 5 km depth. The wells have been hydraulically stimulated for enhanced fluid permeability during the project. The 5 km depth mentioned corresponds to temperatures of ~200 degrees Celsius.

The highest magnitude event observed during the stimulations is M_L2.9 (Gaucher et. al. 2015). In total the stimulations for the boreholes were conducted in eight different stimulation periods during which thousands of microseismic events were observed each time.

Considering the achieved fluid flow the Soultz area basement rock involves interconnected fractures and large faults naturally and their presence affects the fluid flow together with the increased permeability achieved with fluid injection.

When comparing the Soultz project with the ST1 project both have boreholes extending to high depths into crystalline basement. The temperature gradient however is much higher at location of the Soultz EGS project and the temperatures differ greatly.

Unlikely the Basel project the Soultz project's seismic responses were within acceptable limits and according to Gaucher et. al. (2015) the Soultz EGS system was able to produce 2.5 MW of power.

5 ST1 PROJECT

The ST1 Deep Heat company has been developing an enhanced geothermal system for district heating in Espoo, Southern Finland. It is located in close proximity to the Finland's capital city, Helsinki. The goal of the project is to provide deep geothermal heat to local district heating. Because of the location the stimulation has been conducted below quite densely populated area with delicate infrastructure. As a complete geothermal doublet the system will consist of two wells from which the first one (OTN-3) was stimulated for a 7 week period in June and July of 2018. Stimulation was conducted in order to increase the fluid permeability of the crystalline rock at the base of the well. The depth of OTN-3 is 6.1 km and the second well will extend to similar depth and will be stimulated during year 2020. A schematic view of the project can be seen in figure 5.1.

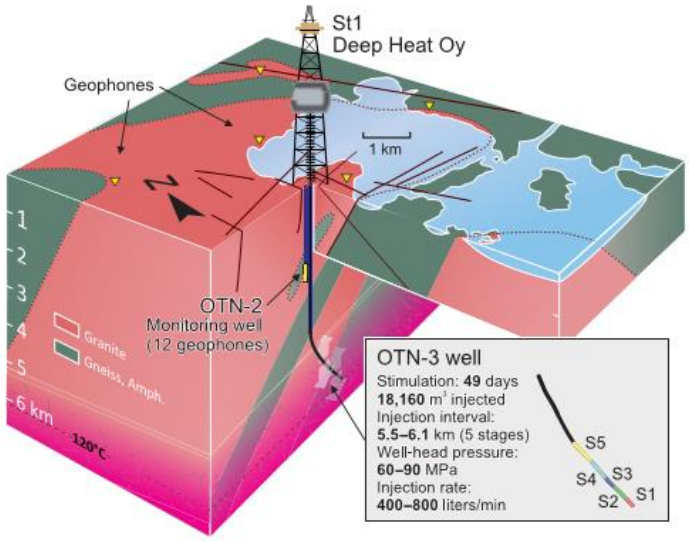

Figure 5.1 Schematic view of the ST1 EGS project. Basic stimulation parameters, depth, temperature and rock types are marked on the figure. Adapted from Kwiatek (2019).

5.1 INDUCED EVENTS DURING THE YEAR 2018 STIMULATION

The first stimulation started on 4th June 2018 and ended on 22nd July 2018 resulting in stimulation length of 49 days. The stimulation was conducted in 5 stages. During the period total of 18.160m^3 of drinking quality water was injected into the well. In total 1357 greater or equal than M_L 0 events were recorded. According to Ader (2019) the overall number of all detected seismic events which were counted as induced events due to the stimulation activity was 8412 and from these events total 6150 were deemed proper for determining locations and magnitudes considering the SNR-ratio. The largest event magnitude determined during the operation was M_W 1.9 according to Kwiatek (2019).

Majority of the largest events and many arbitrarily chosen events taken place during year 2018 stimulation were associated with reverse-faulting mechanism according to Hillers et. al (2018) based on fault plane solutions. This suggests that the reverse-faulting mechanism has an important role in

the seismic response of the stimulated area. Hillers et. al (2018) suggests that in the case of the largest observed events the stimulation reactivated a set of pre-existing faults or shear fractures favouring reverse motion in the local stress field.

The injection rate of the fluid down the hole was usually between 400 l/min to 600 l/min but was high as 800 l/min for few hours during stage 2 and this led to increased seismic activity. According to Kwiatek (2019) the mean well-head pressured ranged from 60MPa to 90MPa during the stimulation. The magnitudes used here are local Finnish magnitudes introduced in Uski & Tuppurainen (1996). Figure 5.2 shows the induced seismicity hypocenters caused by the stimulation. The locations shown have been revised and are not the automatic locations. Figure 5.3 shows the b-value and magnitude-frequency distribution of the induced events that took place during the stimulation period. Table 1. lists the amount of induced seismic events per fluid injection stage together with the injected fluid volumes and maximum injection pressures.

Table 1, adapted from Ader (2019):

Stage	Start date	Net injected volume (m^3)	Max injection pressure (bars)	Mean depth (m)	Number of events			
					$M_L \geq 0$	$M_L \geq 1$	$M_L \geq 1.2$	$M_L \geq 2.1$
1	4 June 2018	3783	890	6056	173	5	3	0
2	16 June 2018	4023	900	5973	280	11	6	0
3	23 June 2018	1537	850	5884	131	8	4	0
4	1 July 2018	4411	860	5771	361	14	9	0
5	12 July 2018	4406	870	5625	412	18	14	0
Total	22 July 2018	18,160	–	–	1357	56	36	0

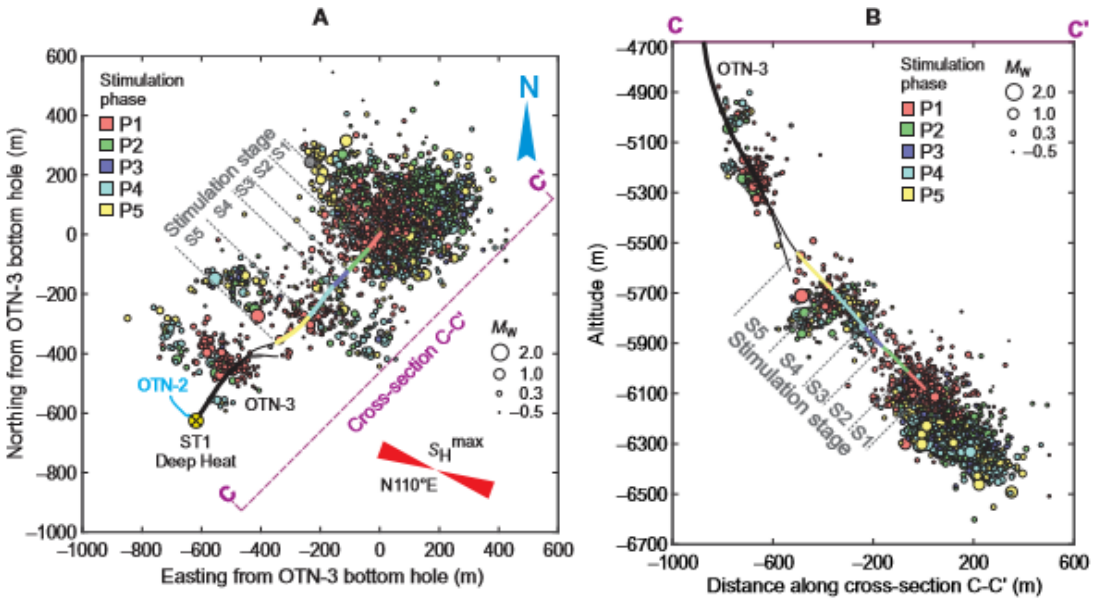

Figure 5.2 Induced seismicity hypocenters during the stimulation. On the left side is a map view of the stimulation area. On the right is a cross-section of the area. Events taken place during different phases of the stimulation period are illustrated in different colours. The well is also divided into sections based different stimulation phases. The sizes of the markers correspond to determined event moment magnitudes. Adapted from Kwiatek (2019).

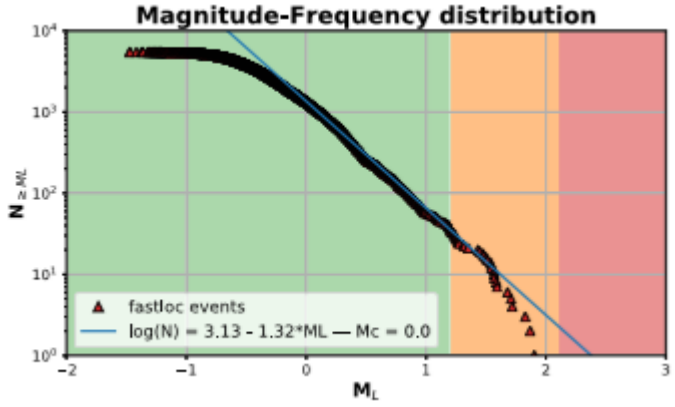

Figure 5.3 Gutenberg-Richter fit and magnitude-frequency distribution of the induced seismic events. G-R fit was applied only to events with $M_L \geq 0$. For the b-value a result 1.32 was estimated. In addition the magnitude thresholds for the alerts are marked with their respective colours. None of the events triggered the red alert. Adapted from supplementary material of Ader (2019).

5.2 TLS FOR THE ST1 PROJECT

The traffic light system used during the first stimulation period of the ST1 project is described in Ader et al. (2019). The data underlying the TLS was collected by 12 3-component seismometers located in shallow boreholes ranging from 300 m to 1150 m depth. Alongside these instruments a vertical array of 12 3-component sensors was installed in a borehole located 10 m away from the OTN-3 well at depths ranging from 2200 m to 2630 m. In addition to these networks 14 accelerometers were located in chosen sites such as places near critical infrastructure. The network of borehole instruments was called satellite network and was used for determining locations and magnitudes for the induced events. The surface accelerometers were called surface network and was used for measuring the amplitudes of ground motions. The TLS system was designed so that it involved usage of both magnitude and ground motion data.

The network was used for baseline monitoring for a period of one month before the stimulation period. The satellite network was used for post-stimulation monitoring for 6 months after the end of the first stimulation period and the surface network was used for 2 months after the stimulation (Ader et al. 2019).

As mentioned earlier in the chapter considering traffic light systems the TLS designed for the ST1 project involved the three commonly used alert levels: green, amber and red alert. The meanings and operations associated with each colour together with the thresholds were following:

Green: In green condition the stimulation process is carried on normally as planned. This involves confirming that the network stations are active and transferring data as expected. This condition is active when the surface stations experience low level of peak ground velocity. Depending on the instrument location this corresponds to values of less than 0.3 mm/s or 0.13mm/s.

Amber: In amber condition the TLS has reacted to an exceedance and a notification, documentation and evaluation of possible actions have been triggered. Amber alert can be triggered by surface vibrations which could be felt in some places in the vicinity of the event, but no structural damage would be expected. This condition is activated when the peak ground acceleration (later PGA) meaning the maximum ground acceleration measured at the location during the event reaches 1mm/s in the surface network alongside an automatically located seismic event near the well of automatically determined magnitude of $M_L \geq 1.0$. An observed event of $M_L \geq 1.2$ triggers the amber condition with or without the PGV observation exceedance.

Red: in red condition exceedance has occurred according to the TLS and the immediate stop of the stimulation process and the well bleed-off option is triggered. Also a notification of the observed event and confirmation considering the stop of operation are triggered. The measures taken would also be documented. After the red alert the stimulation would continue only after approval from the local authorities. The threshold for red condition however is determined to be still so low that no structural damage would be expected at the threshold limit. The red condition would activate if the PGV exceed 7.5 mm/s value in the surface network. Considering magnitude a seismic event near the well of automatically determined magnitude of $M_L \geq 2.1$ would trigger the red alert with or without exceedance of PGV values.

In addition, the timetables for informing different parties involved in the project were determined in the TLS after triggering amber or red condition. The system involving both magnitude and PGV data was used in order to reduce false positive and false negative triggering of the TLS. It is mentioned that empirical ground motion prediction equation from Douglas et al. (2013) and from the Institute of Seismology of the University of Helsinki were used in determining the used PGV threshold values.

6 DATA ACQUISITION

6.1 SEISMIC EVENTS USED IN THE STUDY

In total 21 induced seismic events that occurred during June and July of 2018 near Otaniemi ST1 Deep Heat well were chosen for this study. The events were chosen based on estimated size received in daily ISUH analysis and estimated magnitudes received from the ST1DH. The event origin times, hypocentre locations and magnitudes are listed in Appendix B.

6.2 SEISMIC STATIONS

During the hydraulic stimulation in June and July 2018 a wide range of seismic instruments were active around the Otaniemi drill site in the Espoo and Helsinki area. The data gathered for this study involves data from seismic stations installed by the Institute of Seismology from University of Helsinki (ISUH) and from the ST1 Deep Heat Oy (ST1DH). The seismic monitoring network installed for the purpose of monitoring the stimulation phase consisted from in total about 100 geophones deployed by the ISUH. Most of the geophones were deployed as arrays but the geophone network also involved single stations. ST1DH gave access to data from the 12 semi-permanent borehole seismometers in the Espoo and Helsinki area. The instruments for monitoring the ST1DH project are located within 10 km of the EGS well.

In addition to the stations deployed for the monitoring of the EGS project data from 5 ISUH broadband HEL seismic stations in the Helsinki area was used. Also data from the nearest stations of the permanent Finnish seismological network was utilized when possible.

Full list of station used in the study alongside their coordinates and elevations can be found in the Appendix A.

Since the stations consist of a wide range of instruments each “type” of stations will be described more precisely. Figure 6.1 shows the locations of the stations in the Espoo/Helsinki area.

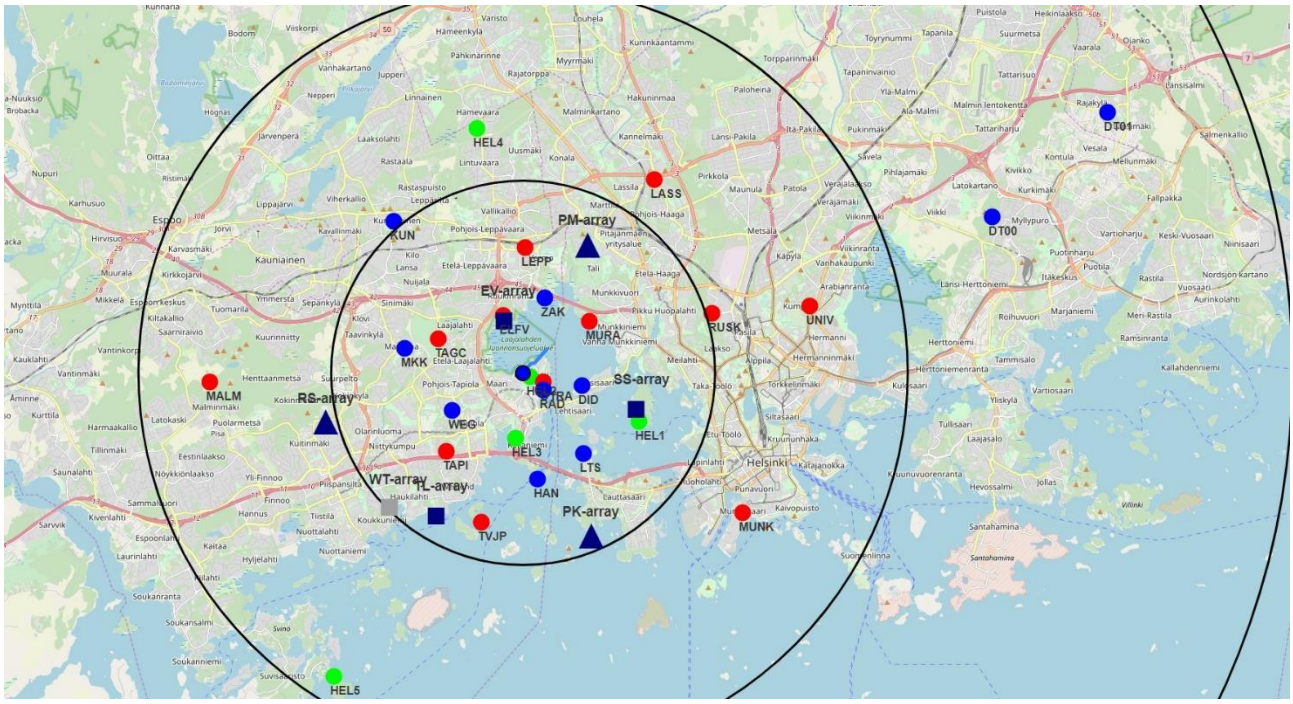

Figure 6.1 Seismic station locations. Red markers correspond to the ST1 borehole stations, green markers are the ISUH HEL-stations and dark blue triangles and squares are arrays consisting of geophones. Blue circles are single geophone stations. WT-array marked with grey was not operational during the stimulation period. The black circles correspond to distances of 5 km, 10 km and 30 km from the ST1 Deep heat well.

6.2.1 Geophone stations and arrays

As total the array network consists of roughly 100 geophones. The geophones are organized mainly in three large arrays which consist of nominally 25 individual geophones. There are also three smaller arrays consisting of four individual geophones and eight single geophones without being involved in an array.

The areas where the three 25 geophone arrays were installed were suburban, undeveloped and for most part tree-covered. Generally the sensors were placed in the thin layer of soil covering ubiquitous bedrock. The locations of the geophones were estimated by using a handheld GPS device.

The instruments are 4.5 Hz PE-6/B-geophones connected to DATA-CUBE3 digitizers with a recording frequency of 400Hz. The cubes were powered with batteries, which were changed in sufficient intervals during the operation. The stations recorded their data continuously on Secure Digital High Capacity cards.

6.2.2 ST1 borehole stations

The ST1DH installed a satellite network consisting of 12 3-component borehole seismometers having 500 Hz sampling rate and installation depths varying from 240 m to 1150 m. The distances from the EGS site vary from 0.6 km to 8.2 km. There was also vertical borehole array consisting of 12 seismometers in the OTN-2 well, but the data of the array is not used in this study.

6.2.3 HEL stations

ISUH HEL stations consist of Nanometrics Compact 3-component broadband seismometers with a sampling rate of 250Hz. In total there are five HEL stations and they are located within 10 km radius of the EGS site.

6.2.4 Permanent station of the Finnish seismological network

In many cases considering the size of the chosen induced events they could be seen in data of the stations belonging to the permanent Finnish National Seismic Network (some events could also be observed and picked in the data of nearest stations of the Estonian seismic network).

The permanent stations having “picks” for P- and S-wave arrivals and in some cases amplitude records are: MEF, NUR, PVF, ARBE, FIA1, VJF, EE08, EE01, RAD, KEF, KAF, KPF, RUF from which the nearest MEF, NUR and PVF are used for almost all events. The stations work at 100-250Hz sampling frequency.

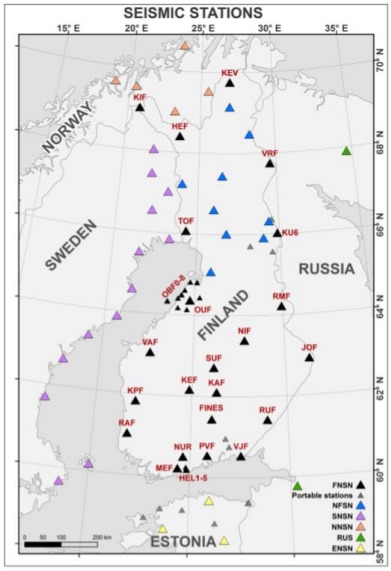

Figure 6.2, map of seismic stations of the FNSM. Nearest seismic stations of the neighbouring countries are also illustrated on the map. Figure adapted from Kortström et al. (2018).

7 DATA PROCESSING

The data processing of the events in this study consisted of two steps. The first step was the determination of the locations of the hypocenters and magnitudes for each event. This was done by picking the arrival times of P- and S-waves and associated amplitude for each of the station records. This step was completed with use of the Geotool software. The second step was data processing with GNU Octave for the calculations using the values obtained from the event locating and amplitude determination. The data recorded by the instruments were corrected for instrument response before usage in Geotool software.

7.1 GEOTOOL

The Geotool software is used in the daily seismic analysis at the ISUH. Geotool is a software system which allows displaying, manual interaction with and processing of seismic data. Originally Geotool was developed by Alexandria Laboratories and the Center of Seismic studies in the 1990s for easy and convenient display and analysis of data from seismic stations. In 2006 and 2007 the software was rewritten for most parts with C++ programming language (Geotool Software User Guide, 2016). The software allows processing of waveform data recorded by for example with seismic stations. The waveform data can be picked for different seismic phase arrivals and amplitudes can be determined from the waveforms. The software package includes tools for waveform processing such as filtering. The waveforms can be used in magnitude determinations and event location determination when Geotool is connected to databases enabling such actions. In ISUH paikka-ohjelma (mentioned in chapter 2., section 13.) is used with Geotool for the magnitude and location estimations of the seismic events.

7.2 GNU OCTAVE

GNU Octave is a software which features a high-level programming language. The software is mostly used for numerical computation. The Octave language can be considered as “open version” of the widely used MATLAB package. GNU Octave is free software under the terms of the GNU General Public License.

Octave was mostly used for the data processing after receiving the event related information from the Geotool and Paikka-program as Nordic-files which consist of event origin time, hypocenter, azimuth gap and magnitude, P- and S-wave arrivals with residuals from theoretical travel times and with determined amplitudes and the amplitude associated frequencies. The arrivals and amplitudes are listed for each station having a record of the seismic event.

For easy computations the needed data was extracted from the Nordic-files into a form where they could be more easily used with the Octave code. The extraction was conducted by a program written with Octave. The numerical data gathered was used for the results of this study.

Figure 7.1 shows the workflow from the recording of the data to the form used in the calculations.

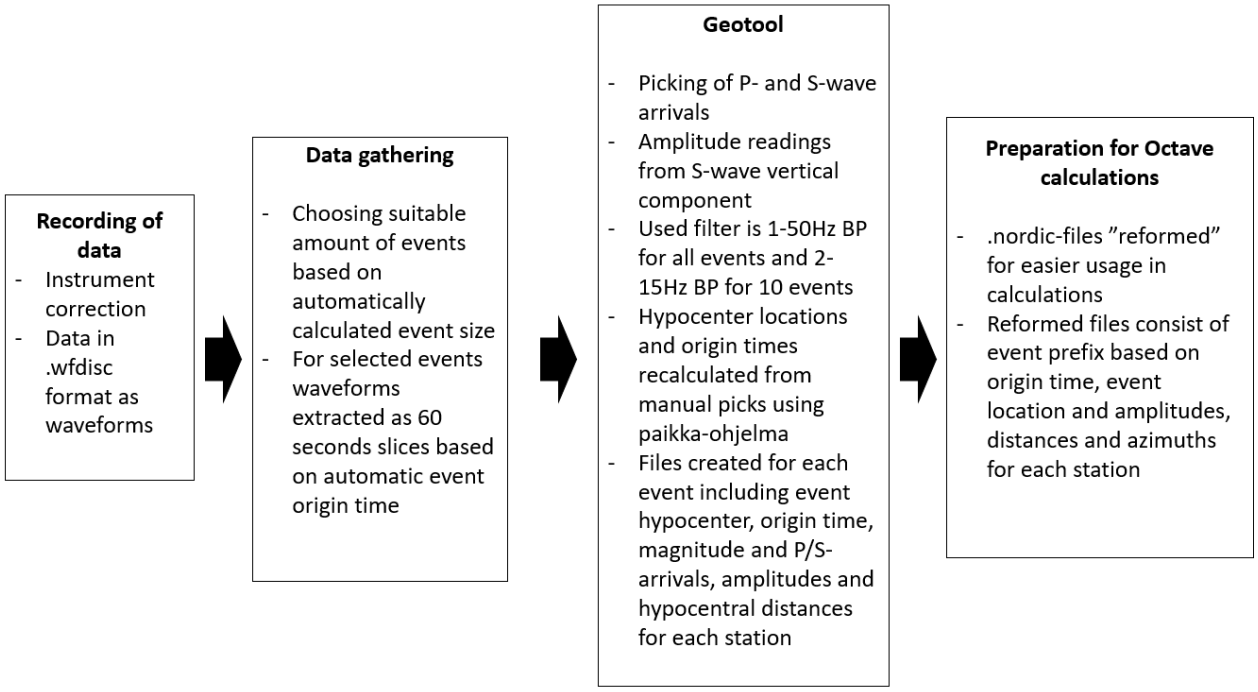

Figure 7.1 workflow from the raw data to the data form used in the calculations.

8 RESULTS

8.1 INFO

Data from 21 induced seismic events that took place near the ST1DH well In Espoo, Finland during the summer 2018 stimulation of the well are used in this section. The seismograms of the events were picked for P- and S-wave arrivals and for amplitude (from S-wave) records with the Geotool software.

For the 21 events the filter mainly used during the Geotool usage was 1-50Hz Bandpass filter chosen to remove noise from the data, but still keep the amplitude information of the near-source events reasonably undiminished. In addition 10 of the 21 events were also picked for the amplitude values with 1-15Hz Bandpass filter which is most commonly used in the daily seismic analysis in the ISUH.

The events are named based on their origin time, day of year, and year and each event has a unique prefix based on those parameters. The prefixes of the events are listed below:

2018162052548, 2018171001230, 2018171232614, 2018172175518, 2018174085934, 2018180040100, 2018180094138, 2018181065239, 2018186070100, 2018187084836, 2018188173124, 2018189173537, 2018193142500, 2018194133411, 2018197172535, 2018199104200, 2018199224500, 2018200105407, 2018200105452, 2018204220258, 2018220155710

Full list of chosen events alongside their magnitudes, origin times and hypocenter locations can be found in the Appendix B.

8.2 MAGNITUDES

For most part the event and station magnitudes are calculated based on the received amplitude values based on formula from Uski (1996):

$$M_L(HEL) = \log(A) + 1.42 \cdot \log(R) + 0.00017 \cdot R + 0.148 + S \qquad (29)$$

where R is the hypocentral distance (km), S is station correction (in practice it is relatively small compared to other factors) and A is the synthesized Wood-Anderson trace amplitude (half of the peak-to-peak amplitude in mm) measured from the vertical component of the S-wave on the seismogram.

For making the amplitude records determined with Geotool software usable with the formula without the conversion into synthesized WA-data the log(A) component can be expressed as:

$$\log(A) = 0.86 \cdot \log(a) - 2.34 \qquad (30)$$

where *a* is the ground motion amplitude (half the peak-to-peak amplitude in nm measured from Sg/Lg wave maximum on original seismograms). A quite similar approximation for synthesized WA amplitudes is used by Alsaker (1991).

The approximation's purpose is to reduce the amount of work and computation needed in analysis the events which have been measured with modern seismograms.

With the addition of formula (30) the magnitude scale becomes:

$$M_L(HEL) = 0.86 \cdot \log(a) + 1.42 \cdot \log(R) + 0.00017 \cdot R - 2.19 + S \qquad (31)$$

where the notation stays same as in formulas (29) and (30). As a notice, the individual station corrections have not been included in calculations made with Octave but could be easily implemented later if seen as necessary. However there are no specific station corrections available for the non-permanent stations at this time. In any case the corrections are reasonably small when compared to the calculated magnitude values and their differences.

During Fennovoima project in 2010-2013 it was noticed in the ISUH that the relation of the formula (31) does not apply well for near-source data. For recordings that locate below roughly 100-150km from the seismic source additional distance correction was added in order to correct this error. The correction has been in use in ISUH daily seismic analysis since then. The correction is as follows:

If R < 150km then:

$$M_L(HEL) = M_L(HEL) + 0.53 - 0.003 \cdot R \qquad (32)$$

For the records where R is less than 150km (almost all of the seismic records used for this study) formula (31) with addition of (32) was used.

8.3 CALCULATIONS WITH OCTAVE

The ”.nordic”-files commonly used in ISUH for event based information are created with the Geotool software based on the picked P- and S-wave arrivals, determined amplitudes, event hypocenter location and origin time. The files can be read into Octave for the calculations with reasonably simple code and the needed information can be extracted into a format much more convenient to work with considering numeric calculations. The calculations considering magnitudes were conducted using this kind of method since the files produced by Geotool or Paikka-ohjelma are not very conveniently used directly using Octave.

The usage of Octave allows creation of different plots for illustration purposes and mathematical analysis of results together with testing of effects of different magnitude formulas. Octave is also used for determining individual station azimuths to be used in calculations when needed.

The Octave code reads the Nordic-file and extracts the needed information such as station IDs and corresponding amplitudes and periods and the information considering the hypocenter location alongside azimuth gap.

List of stations and their locations is used to calculate the hypocenter distances from the event location. The distances are approximated to be sufficiently small for using a formula where the path of the seismic wave does not curve because of the seismic wave velocity gradient. Most hypocenter distances end up being less than 10 km. For the further away stations, the magnitude determinations made with the Octave code reasonably well agree with the determinations that have been made with the Geotool and the Paikka-ohjelma even when using the mentioned approximation. This seemed to apply even to the records of the permanent station of the Finnish seismic network which are located much further away than the mentioned 10 km from the event source.

The formula (31) with addition of formula (32) is used for most of the magnitude calculations. If different magnitude formula is used it is clearly stated in the text.

The total magnitude of an event is calculated as the mean of all station magnitudes and uncertainty is estimated with standard deviation of the magnitude values. With the involvement of the arrays consisting of maximum 25 stations in practically same place the way how they are included in the calculation is generally done by taking the median value of the magnitude records for the array. If the effect of using mean or other methods of involving arrays in the magnitude calculation is used it will be stated clearly in the text.

Figure 8.1 shows the different kinds of procedures done with the data.

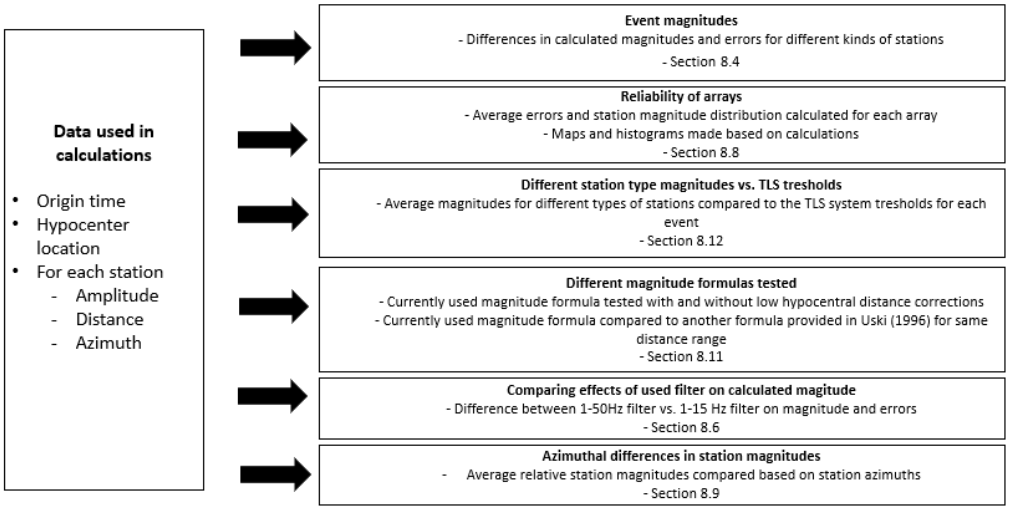

Figure 8.1 Usage of the processed data and the procedures done for the results.

8.4 MEAN OF STATION MAGNITUDES PER EVENT

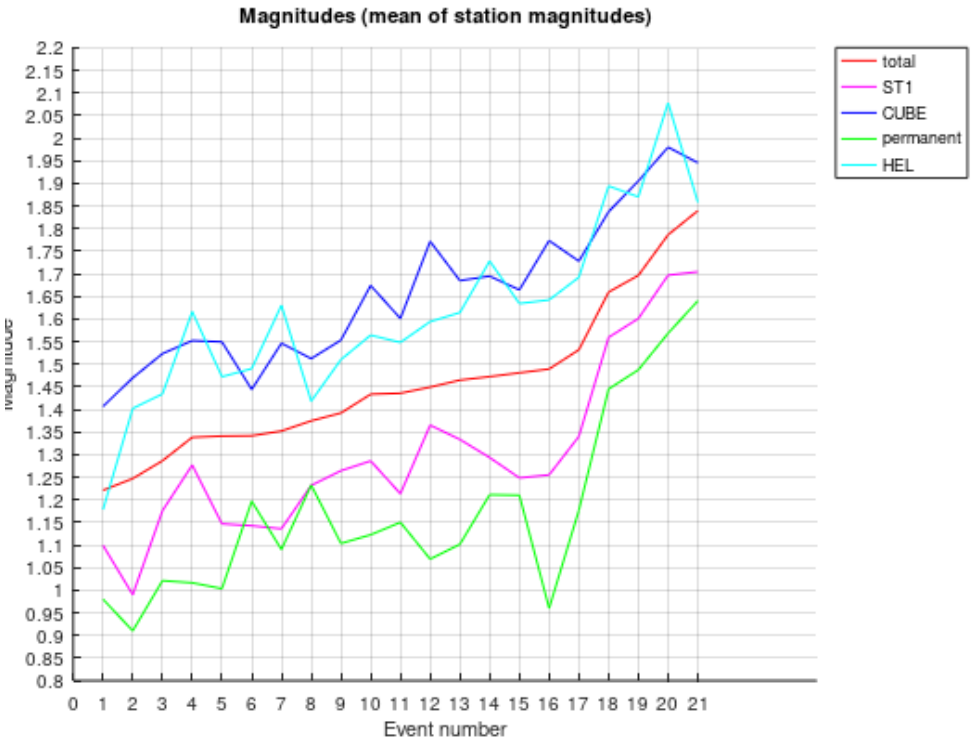

Figure 8.2 Event magnitudes and means of each station type magnitudes illustrated for each event. The events are sorted in ascending order based on the calculated event magnitude. No chronological order can be seen in the figure. The trends in estimated magnitudes between different kinds of seismic stations used can be seen clearly. Individual event numbers can be seen on the x-axis and local magnitude (M_L) is seen on the y-axis. The stations are divided in 4 subgroups and the corresponding colours can be seen on the legend on the right side. Red line corresponds to the total event magnitude, violet line to the ST1 borehole station magnitude, blue line to the Cube array and station magnitude, green line to the permanent seismic network station magnitude and cyan line to the HEL-station magnitude.

Based on the results it seems that there is clear difference between the magnitudes calculated based on different station type records. On average it appears that the surface-located stations such as the

cube stations and arrays and HEL stations deployed by ISUH seem give higher magnitude values. The ST1 stations located in boreholes seem to give lower magnitude values alongside the permanent stations of the Finnish seismological network. It should be noted that the permanent station records were filtered with 1-15Hz filter compared to the rest of the records filtered with the 1-50Hz filter in order to minimize the amount of amplitude cut happening if close distance data is filtered by removing high frequencies. The cube stations contribute to the total magnitude as one station per array which is chosen to have the median value of the particular array in order to avoid the cube station controlling the total magnitude just because of their great number.

For most of the cases the magnitudes from all station types seem to agree with the relative size between the events which is desirable when considering the reliability of the magnitude determination. The disagreements between the relative sizes between the events appear to be between borehole stations + permanent stations of the Finnish seismic network and the cube stations + HEL stations.

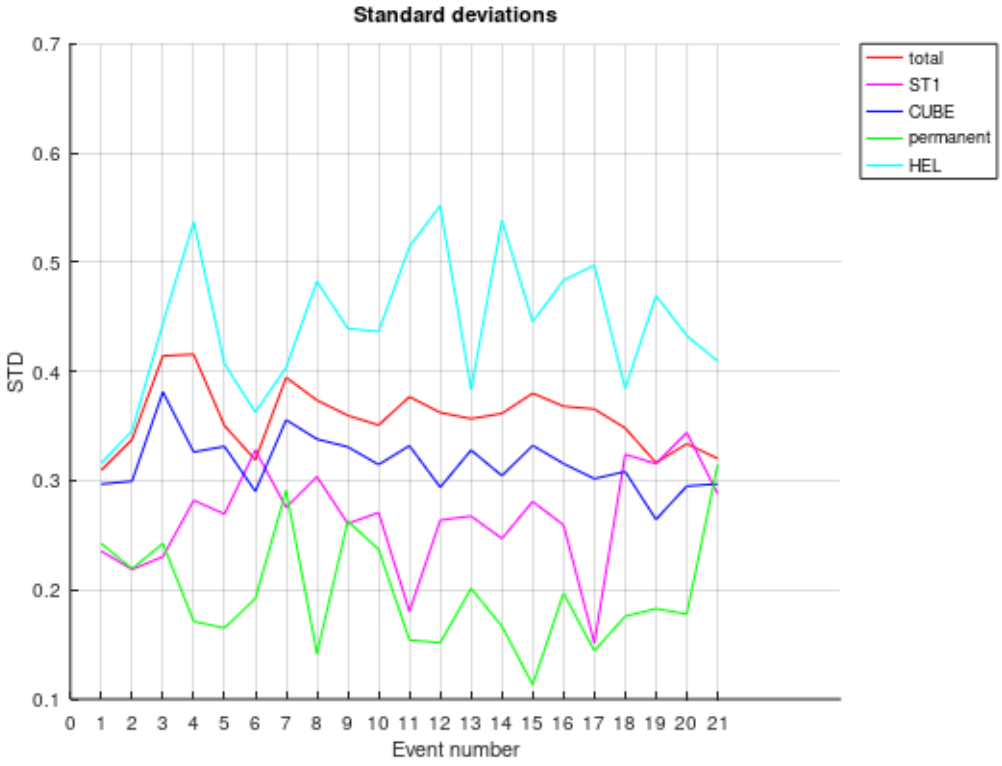

Figure 8.3 Standard deviations of the magnitude records for each station subtype. Individual event numbers can be seen on the x-axis and the standard deviation of the local magnitude (M_L) values is seen on the y-axis. The stations are divided in 4 subgroups and the corresponding colours can be seen on the legend on the right side. It can be seen that the different station subgroups experience different amounts of uncertainty considering the magnitude values. There appears not to be clear trend on the STD based on the event size. Red line corresponds to the total event magnitude STD, violet line to the ST1 borehole station magnitude STD, blue line to the Cube array and station magnitude STD, green line to the permanent seismic network station magnitude STD and cyan line to the HEL-station magnitude STD.

The HEL stations seem to have the highest STD values across all events. Cube arrays and stations tend to have second highest STD values of the station types. Therefore the station types with highest magnitude estimations seem to have higher STD values as well. The permanent station results with 1-15Hz BP filtered records give lowest STD values. The STD values seem to vary significantly from event to event and seem not to be related to the calculated magnitude of the event in question. The STD variation between each event seems to be lower with the cube stations, which is most likely caused by their great number in comparison with the other station subgroups. The locations of the individual stations of the low quantity subgroups could easily also affect the average STD values when considering the focal mechanisms and radiation patterns of the events.

In figure 8.4 the station subtype average magnitudes are plotted against the calculated event magnitude.

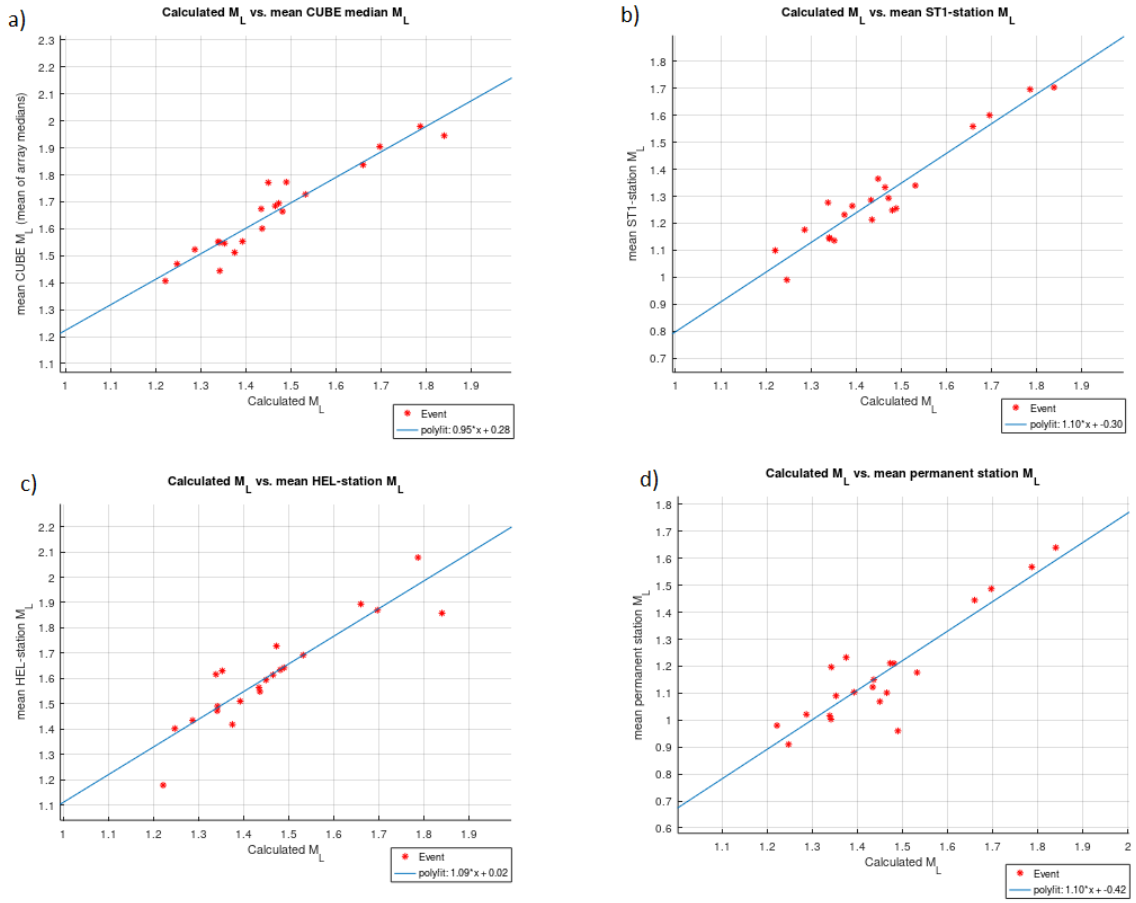

Figure 8.4 Event magnitude compared to the mean magnitudes of different station subgroups for each event. Red dots on the graphs correspond to the magnitude estimates. Mean total magnitude is shown on the x-axis and the corresponding station subgroup magnitude is shown on the y-axis. The blue line is fitted to the data based on least-squares method. The station type subgroup for each graph are a) Cube-stations, b) ST1 borehole stations, c) HEL-stations and d) permanent stations of the Finnish Seismological Network.

The different stations type subgroups appear to estimate the relative size of the events well for majority of the events. The permanent stations seem to perform worst, but in defence their involved number per each event is very small compared to other stations types.

8.5 AUTOMATIC INITIAL MAGNITUDE VALUES COMPARED TO THE MAGNITUDE VALUES CALCULATED IN THE STUDY

Table 2. Comparison of the magnitudes received based on the data used in this study versus the automatically picked magnitudes received during the stimulation.

Event PREFIX	Event M_L (median value taken for each array)	Event M_L (mean across all station records)	automatic ST1 station M_L	event M_L vs. automatic ST1 M_L
2018162052548	1,45	1,65	1,32	0,13
2018171001230	1,34	1,49	1,47	-0,13
2018171232614	1,66	1,81	1,83	-0,17
2018172175518	1,34	1,50	1,54	-0,20
2018174085934	1,25	1,46	-	-
2018180040100	1,70	1,87	1,72	-0,02
2018180094138	1,46	1,67	1,59	-0,13
2018181065239	1,47	1,70	1,68	-0,21
2018186070100	1,48	1,71	1.57*	-0.08*
2018187084836	1,43	1,66	1,54	-0,11
2018188173124	1,49	1,72	1,55	-0,06
2018189173537	1,84	1,97	1.9*	-0.06*
2018193142500	1,37	1,51	1,57	-0,20
2018194133411	1,44	1,59	1,41	0,03
2018197172535	1,79	1,94	1,87	-0,08
2018199104200	1,39	1,60	1,50	-0,11
2018199224500	1,34	1,55	1,63	-0,29
2018200105407	1,29	1,44	1,57	-0,28
2018200105452	1,53	1,67	1,71	-0,18
2018204220258	1,35	1,56	1,63	-0,28
2018220155710	1,22	1,34	-	-

Automatic ST1 station M_L is magnitude value taken from excel involving the first magnitudes received from ST1. The mean difference between the magnitudes calculated using all station (considering arrays as one station) and between the initial magnitudes received from automatic initial ST1 event magnitude excel was -0.13 M_L when subtracting the automatic magnitudes from the manual magnitude estimates. For few of the events used in this study there was no corresponding event found in the excel sheet of the initial automatic magnitudes.

8.6 Effect of filtering (1-15Hz vs. 1-50Hz)

The effect of the used filter on the calculated magnitude values will be considered next. The comparison is between 1-50Hz BP filter and 1-15Hz BP filter.

The events picked for amplitude values with both mentioned filters considered in this comparison are:

2018162052548 (M = 1.45), 2018171001230 (M = 1.45), 2018171232614 (M = 1.66), 2018180040100 (M = 1.70), 2018180094138 (M = 1.46), 2018181065239 (M = 1.47), 2018187084836 (M = 1.43), 2018193142500 (M = 1.34), 2018197172535 (M = 1.79), 2018200105407 (M = 1.29)

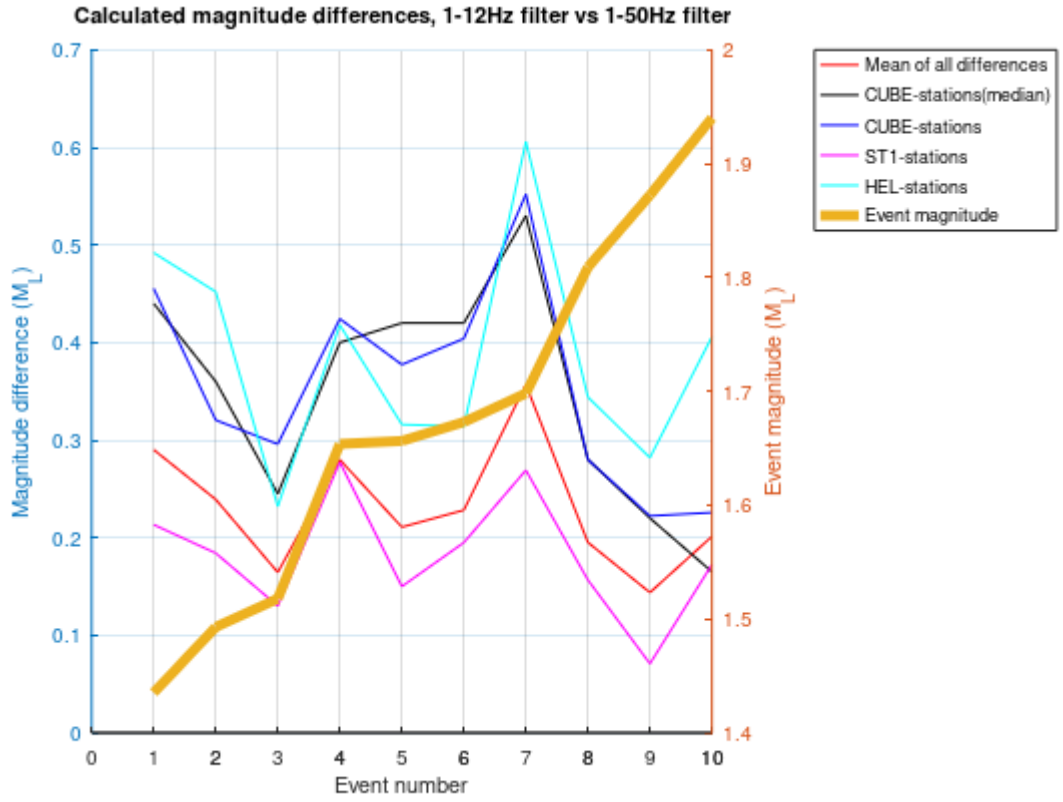

Figure 8.5 The comparison between magnitude values received using 1-50Hz and 1-15Hz filters during amplitude determination. The difference between the received magnitude values is shown on the left side in the y-axis. Positive values indicate that the 1-50Hz filter magnitude is higher than the 1-15Hz filter magnitude. On the right side of the y-axis is the event magnitude. The event magnitude (thick orange plot) is also illustrated on the figure for making the relative size of the events visible (here the event magnitude is calculated simply by taking mean of all station magnitudes for the 1-50Hz filter). The event numbers are sorted in ascending order based on event magnitude. There appears not to be clear relationship between event magnitude and the difference between the magnitudes received using different filters. Red line corresponds to the total event magnitude difference, violet line to the ST1 borehole station magnitude difference, blue line to the mean Cube array and station magnitude difference, black line to the Cube array and station magnitude difference (median value used for arrays) and cyan line to the HEL-station magnitude difference. Since the permanent stations were picked with the 1-15Hz filter in both cases they are excluded.

The size of the magnitude difference caused by the filter seems not to correlate the with the calculated magnitude of the event. The event with the highest difference has only average magnitude compared to others and some of the largest events in the comparison have average or even less than average calculated magnitude difference.

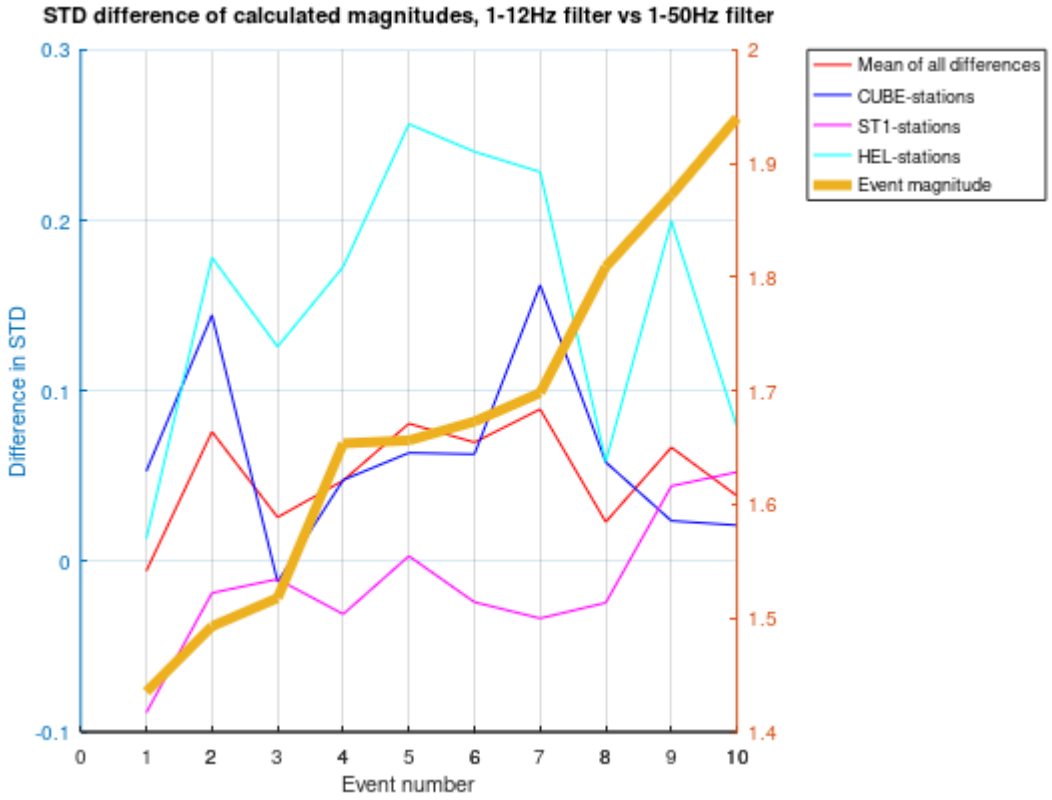

Figure 8.6 The comparison between STDs of the magnitude values received using 1-50Hz and 1-15Hz filters during amplitude determination. The difference in the STD between the received magnitude values is shown on the left side in the y-axis. Positive values indicate that the 1-50Hz filter STD is higher than the 1-15Hz filter STD. Since the permanent stations were picked with the 1-15Hz filter in both cases they are excluded. On the right side of the y-axis is the event magnitude. The event magnitude (thick orange plot) is also illustrated on the figure for making the relative size of the events visible. The event number are sorted in ascending order based on event magnitude. There appears not to be clear relationship between event magnitude and the difference between the STDs of the magnitudes received using different filters. Generally the 1-15Hz filter lowers the STDs which can be caused by both the lower noise values and lower picked amplitudes. Red line corresponds to the total event magnitude STD difference, violet line to the ST1 borehole station magnitude, blue line to the mean Cube array and station magnitude STD difference, black line to the Cube array and station magnitude STD difference (median value used as station magnitude for arrays) and cyan line to the HEL-station magnitude STD difference.

Differences in standard deviations in calculated magnitudes between events picked with filters 1-50Hz BP and 1-15Hz BP. Positive values indicate that the 1-15Hz filter records have higher standard deviation.

The standard deviations seem to be somewhat higher on average in the case of the 1-50Hz filter usage. Especially when considering the HEL stations and arrays. The STD differences do not really show a consistent pattern in the sample of the 10 events.

8.7 MAPS OF INDIVIDUAL ARRAYS

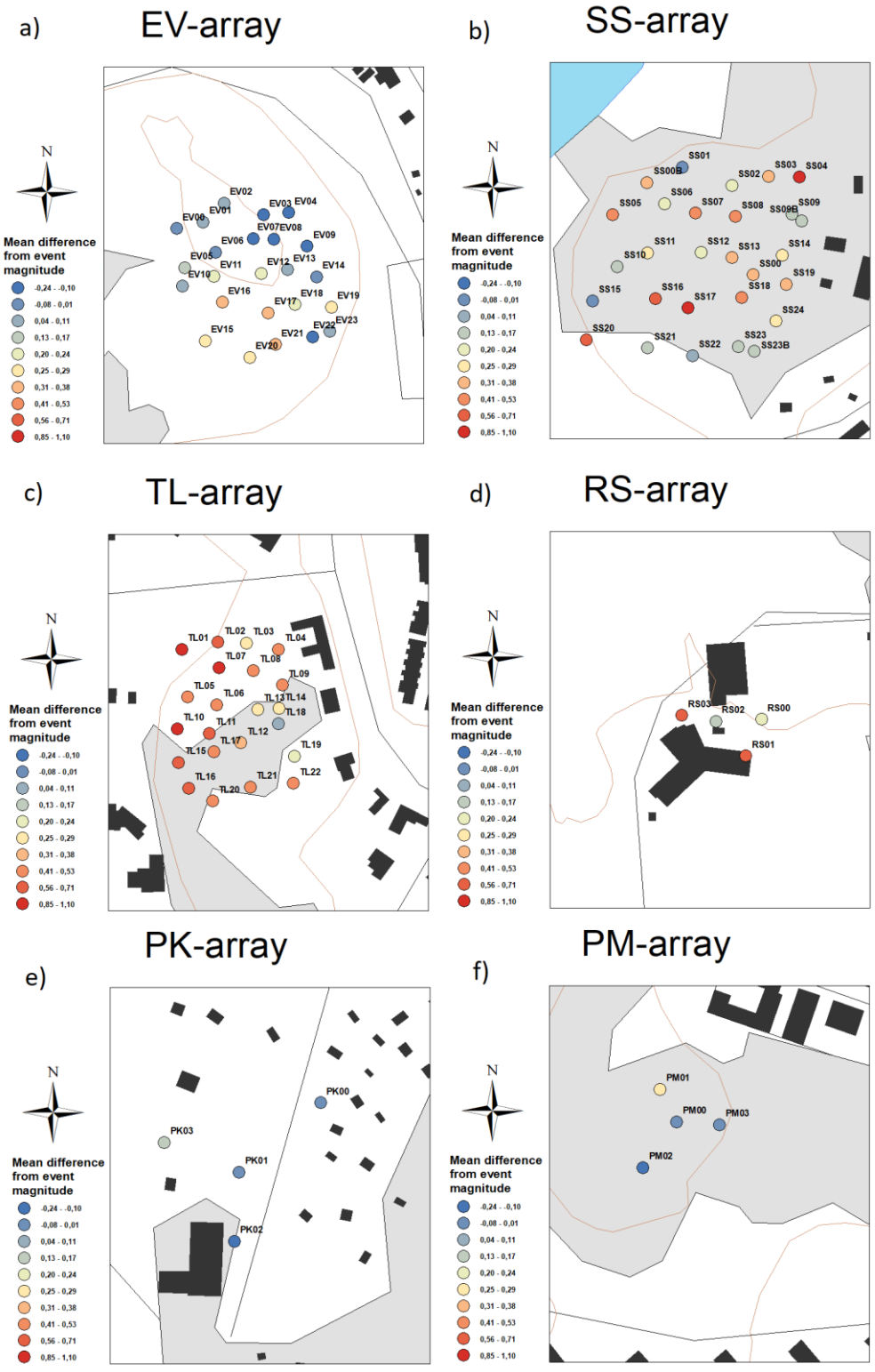

Figure 8.7 Differences in average station magnitudes inside each array between different cubes. The individual cube magnitude estimates are compared to the event magnitude calculated using all stations of the network. Cubes generally overestimating magnitude values are marked with warm colours. Cubes underestimating magnitude values have cool colours. The values shown are based on difference from the event magnitude. There seems to be clear variation between the average values provided by each cube inside each array. The arrays consisting of namely 25 instruments are a) EV-, b) SS- and c) TL- arrays. Smaller 4-istrument arrays are d) RS-, e) PK- and f) PM-arrays. The names of the arrays are abbreviations of the locations where they are deployed.

An individual array seems to either overestimate or underestimate the event magnitude on average as can be seen from figure 8.7. There are clear differences between different cubes of each array. Some of the cubes experience clearly higher or lower amplitudes compared to others despite belonging to the same array nearly at the same place in the site and being same kind of instruments. It seems that overestimation of the magnitude values is much more common overall than underestimation. The differences between different cubes may be caused by the direct subsurface material properties or perhaps by slight differences in installation of the geophones.

On average the overestimations are of far greater magnitude than the average underestimations. The most sensitive cube overestimates the magnitudes on average with a value of roughly 1 whereas the least sensitive cube underestimated them with less than quarter of that value.

8.8 Comparison of array maps with results of "The 2018 Geothermal Reservoir Stimulation in Espoo/Helsinki, Southern Finland: Seismic Network Anatomy and Data Features"

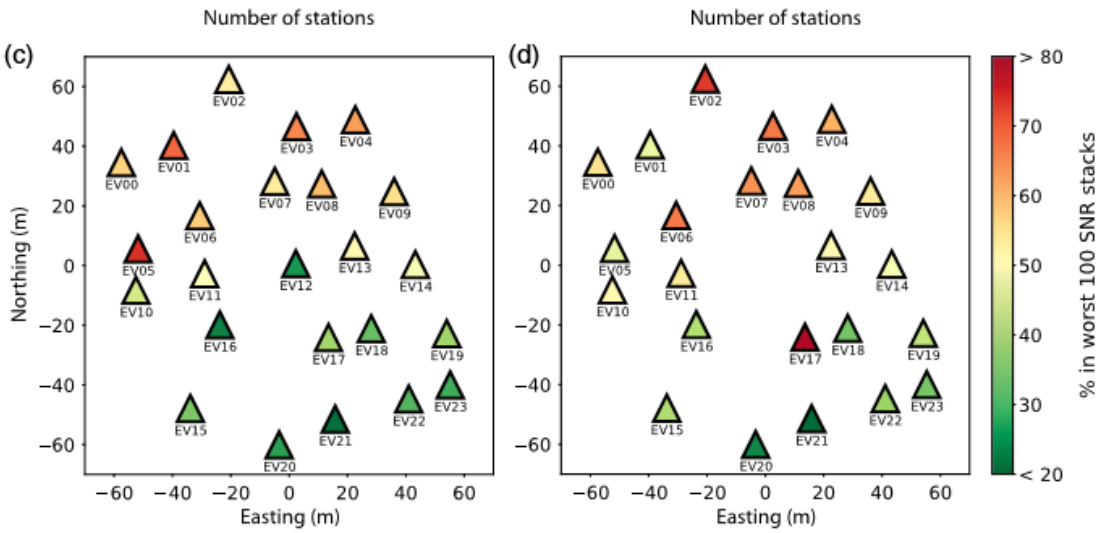

Figure 8.8 Signal-to-noise ratios of the individual stations of the EV-array. Red values indicate bad SNR ratios and green values indicate on average good SNR values. c) shows the statistics from the largest 134 events. d) shows the statistics from the single largest event of M_L 1.8. Figure adapted from Hillers et al. (2020).

The stations having on average largest negative differences from calculated event magnitude seem to be for the most part same as the ones providing worst SNR-ratios on average in Hillers et al. (2020). Same also seems to work another way around. Stations with higher magnitude estimates tend to have better SNR-ratios. This could be related to the direct subsurface under the station and the instruments contact to the medium. The stations deployed in the northern parts of the EV-array

tend to sit on thicker soil layer than their southern counterparts sitting on hard rock directly. The variations in data quality could be due to coupling issues with the subsurface

8.9 AZIMUTHAL DIFFERENCES IN CALCULATED STATION MAGNITUDES COMPARED TO THE EVENT MAGNITUDE

Azimuthal effects of the magnitude differences are shown in figure 8.9. The effects were studied by slicing azimuth range into slices where stations were grouped. Each station type used (here ST1, HEL, CUBE) were compared to their own subtypes mean magnitude for each event. Shown results are mean across all events used in the study. The calculation was tested with different azimuth slice sizes and the 30 degree slices seemed most stable considering results. Tighter azimuth slicing resulted in too low amount of stations per azimuth slice whereas too large slices resulted in dampening much of the azimuthal effects.

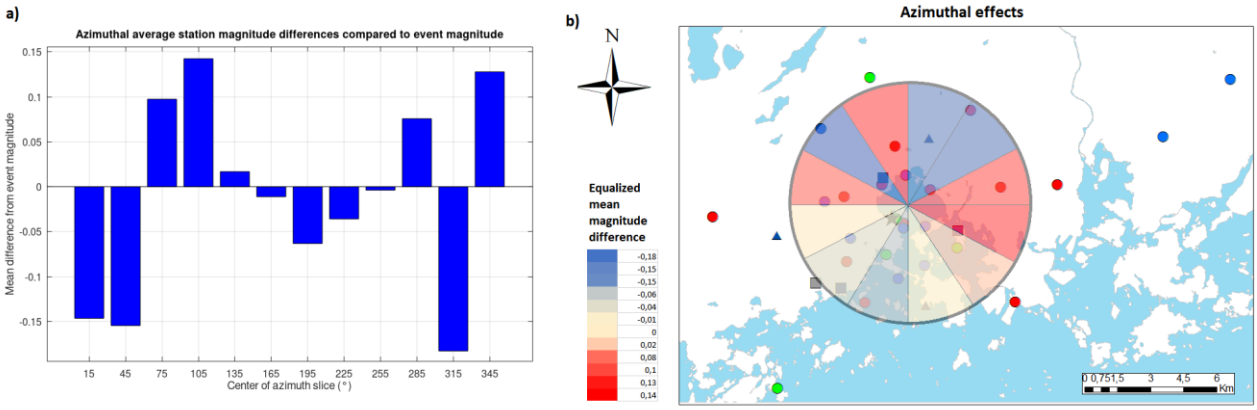

Figure 8.9 Azimuthal average magnitude differences between stations based on the azimuth from the event hypocenters. The circle was divided into 30° slices for the analysis and each station was located into a corresponding slice based on its azimuth. The mean is across all events in the study. The station subtypes involved are ST1-, HEL- and cube stations. The calculation was conducted by comparing each station to their subtype's mean magnitude for each event and the mean of the mean values of all used station subtype magnitude differences per azimuth slice are shown. On the left side is a bar graph of the received azimuthal effects. Map of the same values is illustrated on the right side. Locations of different station subtypes and EGS site are also marked on the map. There seems to be clear average differences between the calculated magnitudes between different azimuths.

There seems to be clear average magnitude differences between different azimuth slices, but the results are mostly vulnerable to be distortion caused by the fact that the stations and station types are not distributed evenly across all azimuth slices. Also the choice for how many slices are made seems to affect the end result. The way of calculation expects the focal mechanisms of the used events to be reasonably similar. The similarity is noted for the largest events in Hillers et al. (2020).

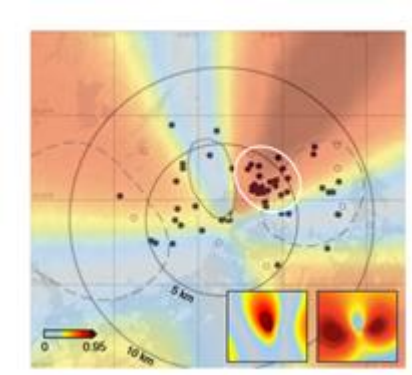

Figure 8.10 SH-wave radiation pattern of the largest induced event during the summer 2018 stimulation. Adapted from Hillers et al. (2020). The filled and open circles correspond to areas where disturbances were reported by the general public during the stimulation. The white eclipse corresponds to the neighbourhood where most of the reports originated from.

In comparison with the figure 5. of Hillers (2018) (Figure 8.10) the average azimuthal station magnitude distribution seems to for some parts follow the SH-wave radiation pattern caused by the largest event. The magnitude is determined from the S-wave so this is expectable. However the uneven distribution of the stations around the Otaniemi EGS well makes accurate interpretation difficult. The area with largest magnitudes appears to be pointed near Munkkiniemi area for both of the maps, even though the direction differs slightly.

8.10 Distribution of errors from calculated magnitude along the cubes of each array

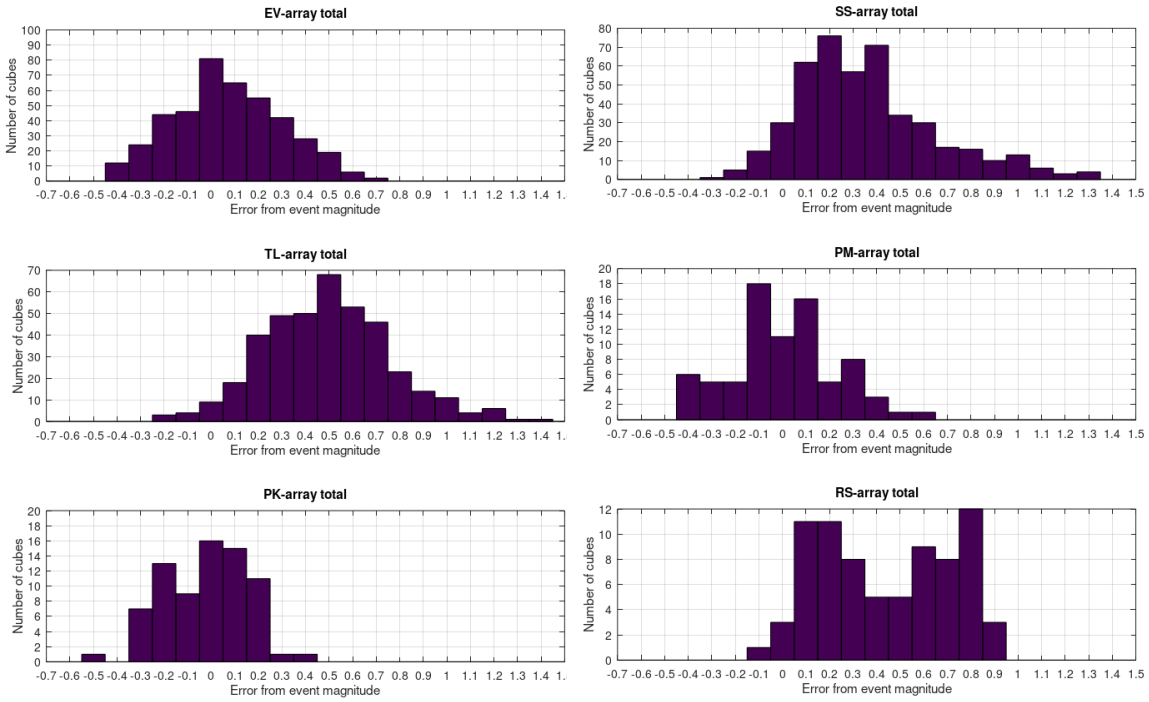

Figure 8.11 Histogram graphs of the sum of the errors from the event magnitude for the cubes of each array based on classification considering the error size. The arrays are marked in the headline of each graph. Each histogram was done by dividing the error into classes based on difference on 0.1 magnitude error and counting the sum of the errors of each class across all events used in the study. The average error distributions between different arrays seems to vary.

Sum of errors from the event magnitudes across all events. Number of cubes is marked on the y-axis. The x-axis shows the error from the calculated magnitude. The histogram was created by grouping values within 0.1 magnitude with each other.

EV- and SS-arrays seem to be the most consistent arrays considering normal deviation to be desirable or expectable if everything is going well considering the measurement. EV-array does follow the shape of normal deviation quite well as can be observed from figure 8.11 while SS-array performs a bit worse. TL-array is clearly tilted to mostly overestimating magnitude values. PM-, PK- and RS are much smaller considering the number of instruments involved, but they seem to also show clear distributions when calculated across all events. PM- and PK-arrays seem to agree with normal deviation, but RS-array has a quite clear M-shape with great quantity of both small and large overestimations.

8.11 EXPERIMENTING WITH DIFFERENT MAGNITUDE FORMULA

Uski (1996) proposes a formula which involves frequency of the amplitude record suggested to be used for events with less than 350km hypocentral distance. However the formula is currently not used in ISUH analysis and the author suggested that it most likely gives less reliable results than the formula commonly used in this study. The formula given in Uski (1996) is written as:

$$M_L(HEL) = \log(A) + 1.27 \cdot \log(R) + (0.00009 + 0.00041 \cdot f^{0.36}) \cdot R + 0.36 + S \quad (33)$$

where R = hypocentral distance (km), S is station correction (in practice it is relatively small compared to other participating factors), A = synthesized Wood-Anderson trace amplitude (half of the peak-to-peak amplitude in mm) measured from the vertical component seismogram and f is the frequency of the wave the amplitude was measured from. Using the same approximation for the WA-seismometer response shown in formula (29). the formula now becomes:

$$M_L(HEL) = 0.86 \cdot \log(a) - 2.34 + 1.27 \cdot \log(R) + (0.00009 + 0.00041 \cdot f^{0.36}) \cdot R + 0.36 + S \quad (34)$$

Including the correction for events with <150km hypocentral (formula 31) distance and combining some of the terms the used formula becomes:

$$M_L(HEL) = 0.86 \cdot \log(a) + 1.27 \cdot \log(R) + (0.00009 + 0.00041 \cdot f^{0.36}) \cdot R - 0.003 \cdot R + 1.45 + S \qquad (35)$$

The formula was tested with all of the amplitude records determined for the 21 events involved in this study using the 1-50Hz BP filter. The formula was not tested with the 10 events picked with the lower frequency (1-15Hz) filter.

In the first figure the calculated event magnitudes received are compared to the ones received with the current M_L(HEL) formula. Both formulas included the correction term for <150km hypocentral distance events. The magnitudes were calculated using the earlier mentioned method, where event magnitude is the mean of all station magnitudes but arrays are considered as one station with station magnitude as the median magnitude value of the cubes of that array.

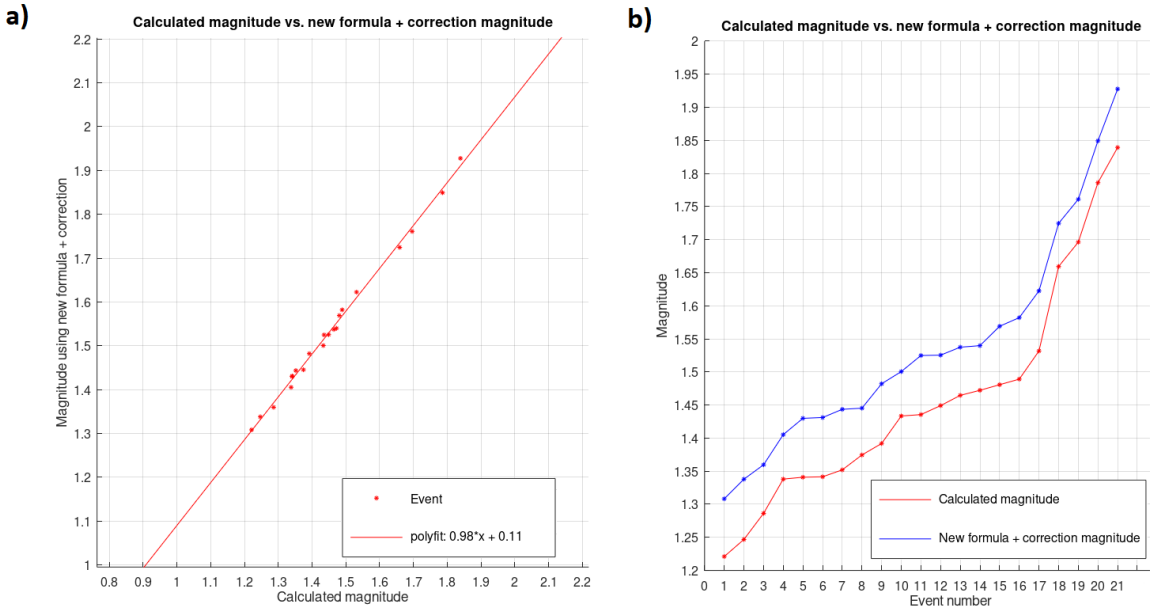

Figure 8.12 Event magnitude versus the magnitude received using the formula (34). On the left side (a) is the event magnitude is on the x-axis and the new calculated magnitude is on the y-axis. The red line is fit based on least-squares method. The formulas seem to agree well on the relative size of the events. On the right side (b) is the absolute values of the magnitude formulas are compared with each other. The event magnitude is plotted with the red and the new calculated magnitude is plotted with the blue line. It appears that the new formula involving the waveforms period overestimated the magnitudes compared to the formula (4).

Based on the results of figure 8.12 it appears that the frequency involving formula estimated the event magnitudes to be slightly higher than the commonly used formula. The amount of overestimation depends on individual event, but it tends to be less than or roughly equal to 0.1 magnitude units. Considering that in Uski (1996) no events with short hypocentral distances where used the results are surprisingly consistent even when considering that the frequencies for the waves

from which the amplitudes have been picked have most likely been much higher than for the cases used in the derivation of the magnitude formulas in Uski (1996). As a notice the low distance correction shown in formula (4) is applied for both of the used formulas.

The effect of the formula (34) on individual station subgroup magnitudes was not tested further since the periods given in the ".nordic"-files based on the waveform where the amplitude records was taken are reasonably close to each other between the different station subtypes.

8.12 TLS SYSTEM

In this section the magnitudes calculated with different methods and the mean station type magnitudes will be compared to the red (M = 2.1) and amber (M = 1.2) traffic light system alert magnitude thresholds. It was done in order to determine would magnitude determination based on certain magnitude types induce more alerts than others. First figure shows the TLS thresholds vs. station magnitudes and event magnitude calculated by using the median magnitude value for each array and otherwise taking mean of all station magnitudes.

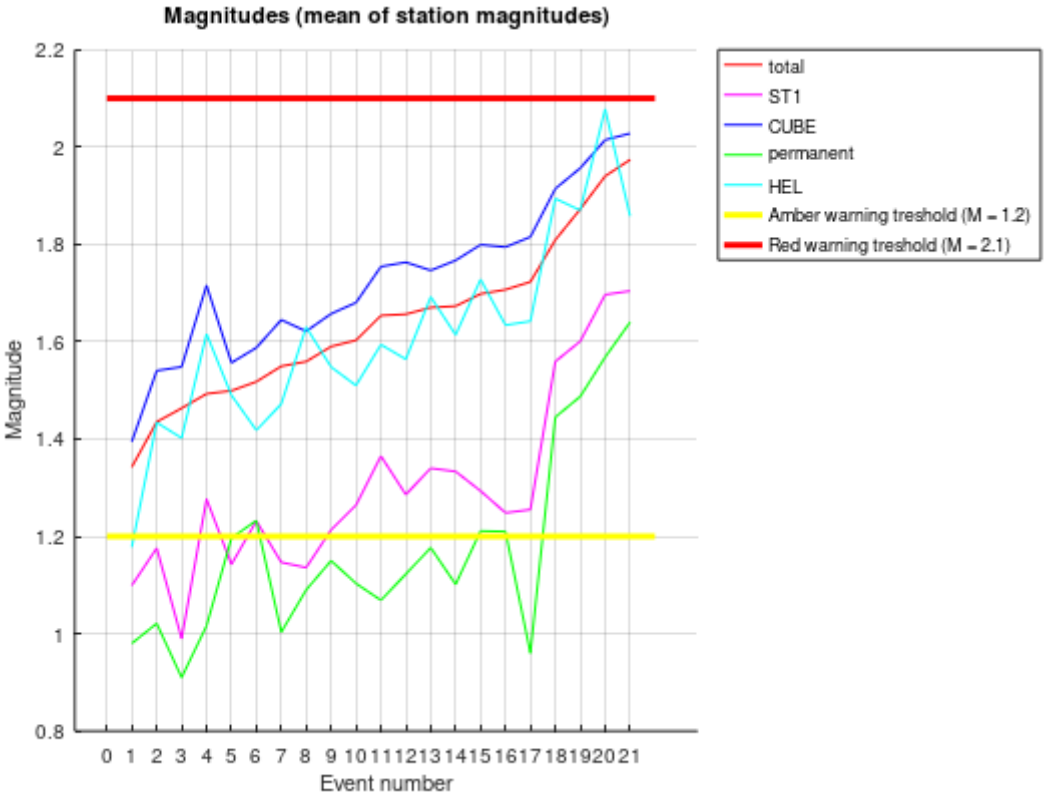

Figure 8.13 Event magnitude and average station type subgroup magnitudes compared to the red and amber warning thresholds of the TLS system. The events are sorted in ascending order based on the calculated event magnitude. Individual event numbers can be seen on the x-axis and local magnitude (M_L) is seen on the y-axis. The stations are divided in 4 subgroups and the corresponding colours can be seen on the legend on the right side alongside the information from the TLS warning thresholds. The red warning thresholds corresponds to M_L 2.1 and the amber warning to M_L 1.2. It appears that even by using only the stations of the most sensitive subgroup the red warning threshold would not have been breached. There appears to be few cases in which by using only selected station type subgroup the amber alert could theoretically have been avoided.

Though already noted in the section 4 of this chapter that certain station types tend to overestimate the event magnitudes it still appears that none of them would suggest that even a single event would be large enough to trigger the red TLS alert. However when considering the threshold for the yellow alert it seems that the average magnitude calculated using ST1 borehole stations undercuts the threshold for some events for which most of the stations and total event magnitude consider it to be triggered.

The permanent station magnitude appears consider roughly half of the events to undercut the amber alert threshold. It appears that cube arrays, single cube stations and HEL-stations would trigger the amber alert for every event in this study as does the event magnitude based on all station records.

For the figure 8.14 the event magnitude is calculated taking mean of all station magnitudes, including array stations as single stations. All other parameters not considering the cube arrays remain the same as in the figure 8.13.

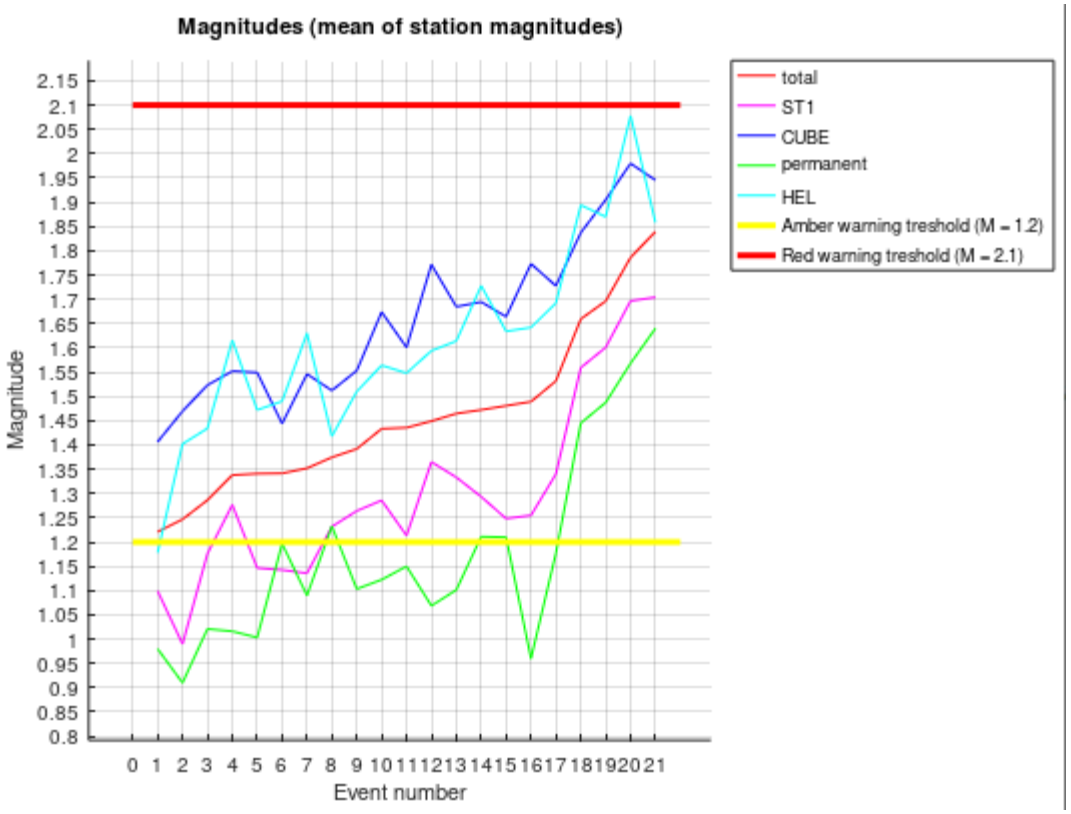

Figure 8.14 Event magnitude and average station type subgroup magnitudes (by taking mean of all individual station magnitudes) compared to the red and amber warning thresholds of the TLS system. The events are sorted in ascending order based on the calculated event magnitude. Individual event numbers can be seen on the x-axis and local magnitude (M_L) is seen on the y-axis. The stations are divided in 4 subgroups and the corresponding colours can be seen on the legend on the right side alongside the information from the TLS warning thresholds. The red warning thresholds corresponds to M_L 2.1 and the amber warning to M_L 1.2. It appears that even by using only the station of the most sensitive subgroup the red warning threshold would not have been breached. There appears to be few cases in which by using only selected station type subgroup the amber alert could theoretically been avoided.

The same observations hold than with the first figure 8.13 of this section. The magnitude overestimation caused by the inclusion of the arrays as ordinary stations is not great enough to

increase the total magnitude to break any thresholds it did not break in the first figure. In addition the mean magnitude of array magnitudes instead of the median value is not alone high enough to break the red alert threshold for any event.

From these observations it can be said that in theory the usage of particular types of stations could indeed in some cases cause or prevent TLS alert thresholds to trigger/from triggering. However it appears that in this case the alert thresholds are chosen so that many of the highest magnitude events induced by the stimulation tend to stand somewhat in the middle between the two thresholds, a case in which relatively small changes in magnitude calculation do not very easily tip the magnitude estimation over or under either of the chosen thresholds.

From the data provided in figure 8.13 and 8.14 it appears that the stations located in the surface or near it on average come much closer to the upper warning threshold than the stations installed in boreholes. The instrumental differences and the amplification caused by the uppermost soil layer the surface stations are planted in could play a role even after possible instrument response corrections.

9 CONCLUSIONS

In total 21 sufficiently large induced seismic events taken place during the stimulation period in summer 2018 of the Otaniemi EGS well were analysed manually by picking P- and S-wave arrivals and amplitudes in order to locate and determine event magnitudes for the purposes of studying the effects associated with the different types of seismic stations and arrays and the behaviour of the currently in use Finnish local magnitude formula. The results with the magnitude calculations were also compared to the TLS thresholds for the amber and red alerts.

There appears to be clear differences in the average station magnitudes between the different station types. The different types of station involved were borehole stations installed by the ST1DH and HEL-, and cube-stations/arrays installed by the ISUH alongside stations from the National Finnish Seismic Network. The near surface installed stations (cube-stations/arrays and HEL-stations) seemed to estimate the event magnitudes to be higher than the borehole installed ST1-stations. For most of the events studied the stations types agreed on the relative sizes of the events.

Alongside the estimated magnitudes the standard deviations of the station magnitudes also varied between station types with the near surface stations experiencing higher values. However also the sample sizes between different station types must be taken into consideration because there were only 5 HEL-stations compared to for example 12 ST1-stations and cubes totalling more than 100 instruments.

Typically the automated event size estimations made during the stimulation for the TLS system seemed to mostly agree with the manually done event magnitudes for this study. Generally the automatic magnitudes estimated the magnitude values to be a bit higher, but within quite acceptable range, leading to the fact that no alert was avoided due to underestimations for the events involved in this study.

The behaviour and trustfulness of the largest arrays was considered more precisely and there appears to be quite high differences between the cubes of a single array. Across all events it seems that part of the cubes is on average overestimating or underestimating event sizes (mostly overestimating). For some arrays the errors seem normally distributed but also other kinds of distributions were encountered. The site effects and small deployment differences between individual instruments may play a role in this. The cubes with most negative difference seemed to experience worst SNR-ratios in Hillers et al. (2020), however this comparison was made just for one array.

It was also noted that the chosen filter when picking the amplitude values seems to greatly affect the results for this kind of near-source events. One could rather easily lower the estimated magnitudes of the events by filtering out some of the higher frequency content. Filtering however seemed to somewhat lower the STD values of the station magnitudes.

There seemed to be clear azimuthal effects in the average magnitudes experienced by the stations around the EGS well site. However the station of the seismic network are not distributed evenly between the chosen azimuth slices and this might affects the reliability of the result alongside with differences in focal mechanisms of the events. The largest magnitudes appear to point roughly at the direction of the highest concentration of seismic observations by the public.

The currently in use Finnish local magnitude formula appeared to give pretty much similar results with a little bit lower magnitude estimations than the another local magnitude formula with the difference of involving wave periods in the calculations. The formulas were introduced in Uski (1996) and are not created with enough near-source data. However currently there is no local magnitude formula for Finnish area made using suitable amount of near-source data. Both formulas needed the currently used correction for near-source events.

Considering the amber and red alert thresholds used by the TLS system in the ST1DH project the threshold values seemed to be chosen so that the differences between the estimated event magnitudes between different station types or calculation choices would not cause them to be breached and not breached between different choices. The amber alert could have been avoided for very few cases and red alert would not have been breached for any calculation choice or choice of station types involved.

In the future the local magnitude formula could be developed further to perhaps be more suitable for near-source data (particularly the near-source correction could be revised) and the behaviour of different types of seismic stations and effect of station geometries could be studied further for example during the next stimulation period of the ST1DH project. The effect of filtering when picking near-source event magnitudes could be also tested further. In addition the effects of the heterogeneities of the subsurface could be considered more since for the purposes of this study their effects were pretty much neglected in the absence seismic model involving such.

10 ACKNOWLEDGEMENTS

I would like to express my gratitude to my supervisor Gregor Hillers for guiding me through this project. I would also like to thank Tommi Vuorinen and Timo Tiira and acknowledge the help I was provided at ISUH for my thesis work.

11 REFERENCES

Ader, T. *et al.* (2019) 'Design and implementation of a traffic light system for deep geothermal well stimulation in Finland', *Journal of Seismology*. doi: 10.1007/s10950-019-09853-y.

Alsaker, A. *et al.* (1991) 'The ML scale in Norway', *Bulletin of the Seismological Society of America*, 81(2), pp. 379–398.

Bormann, P. *et al.* (2009) *Seismic Sources and Source Parameters*. Deutsches GeoForschungsZentrum GFZ. doi: 10.2312/GFZ.NMSOP_r1_ch3.

Bormann, P. and 2. 1 Physics of Earthquakes and Volcanoes, 2 0 Physics of the Earth (2012) 'New Manual of Seismological Observatory Practice (NMSOP-2)'. doi: 10.2312/GFZ.NMSOP-2.

Bormann, P., Engdahl, B. and Kind, R. (2009) *Seismic Wave Propagation and Earth models*. Deutsches GeoForschungsZentrum GFZ. doi: 10.2312/GFZ.NMSOP_r1_ch2.

Dezayes, C., Genter, A. and Hooijkaas, G. R. (no date) 'Deep-Seated Geology and Fracture System of the EGS Soultz Reservoir (France) based on Recent 5km Depth Boreholes', p. 6.

Eaton, D. W. and Igonin, N. (2018) 'What controls the maximum magnitude of injection-induced earthquakes?', *The Leading Edge*, 37(2), pp. 135–140. doi: 10.1190/tle37020135.1.

Eilu, P. (ed.) (2012) *Mineral deposits and metallogeny of Fennoscandia*. Espoo: Geological Survey of Finland (Special paper / Geological Survey of Finland, 53).

Elst, N. J. van der *et al.* (2016) 'Induced earthquake magnitudes are as large as (statistically) expected', *Journal of Geophysical Research: Solid Earth*, 121(6), pp. 4575–4590. doi: 10.1002/2016JB012818.

Evans, K. *et al.* (2012) 'A survey of the induced seismic responses to fluid injection in geothermal and CO2 reservoirs in Europe', *Geothermics*, 41, pp. 30–54. doi: 10.1016/j.geothermics.2011.08.002.

Gaucher, E. *et al.* (no date) 'Induced Seismicity in Geothermal Reservoirs: Physical Processes and Key Parameters', p. 13.

Gérard, A. *et al.* (2006) 'The deep EGS (Enhanced Geothermal System) project at Soultz-sous-Forêts (Alsace, France)', *Geothermics*, 35(5), pp. 473–483. doi: 10.1016/j.geothermics.2006.12.001.

Giardini, D. *et al.* (2004) *Seismic Hazard Assessment of Switzerland, 2004*.

Grad, M. and Luosto, U. (1994) 'Seismic velocities and Q-factors in the uppermost crust beneath the SVEKA profile in Finland', *Tectonophysics*, 230(1), pp. 1–18. doi: 10.1016/0040-1951(94)90144-9.

Häring, M. O. *et al.* (2008) 'Characterisation of the Basel 1 enhanced geothermal system', *Geothermics*, 37(5), pp. 469–495. doi: 10.1016/j.geothermics.2008.06.002.

Hillers, G. *et al.* (2020) 'The 2018 Geothermal Reservoir Stimulation in Espoo/Helsinki, Southern Finland: Seismic Network Anatomy and Data Features', *Seismological Research Letters*. doi: 10.1785/0220190253.

Hirschberg, S., Wiemer, S. and Burgherr, P. (eds) (2015) *Energy from the earth: deep geothermal as a resource for the future?* Zürich: VDF Hochschulverlag an der ETH Zürich (TA-SWISS (Series), 62/2015).

Hutton, L. K. and Boore, D. M. (1987) 'The M_L scale in Southern California', *Bulletin of the Seismological Society of America*, 77(6), pp. 2074–2094.

Kakkuri, J. and Chen, R. (1992) 'On horizontal crustal strain in Finland', *Bulletin Géodésique*, 66(1), pp. 12–20. doi: 10.1007/BF00806806.

Korja, kosonen (2015) 'Seismotectonic framework and seismic source area models in Fennoscandia, northern Europe', p. 285.

Kortström, J., Uski, M. and Oinonen, K. (2018) 'The Finnish National Seismic Network', *Summary of the Bulletin of the International Seismological Centre*, 52(I), pp. 41–52. doi: 10.31905/59QRNANC.

Kwiatek, G. *et al.* (2019) 'Controlling fluid-induced seismicity during a 6.1-km-deep geothermal stimulation in Finland', *Science Advances*, 5(5), p. eaav7224. doi: 10.1126/sciadv.aav7224.

Lahtinen, R. (2012) 'Main geological features of Fennoscandia', *Special Paper of the Geological Survey of Finland*, 2012, pp. 13–18.

Lay, T. (1995) *Modern global seismology*. Academic Press (International geophysics series).

Lipponen, A. *et al.* (2005) 'Effect of water and geological factors on the long-term stability of fracture zones in the Päijänne Tunnel, Finland: a case study', *International Journal of Rock Mechanics and Mining Sciences*, 42(1), pp. 3–12. doi: 10.1016/j.ijrmms.2004.05.006.

Luosto, U. (no date) 'Structure of the Earth's Crust in Fennoscandia as Revealed from Refraction and Wide-Angle Reflection Studies', p. 14.

Luukas, J. *et al.* (no date) 'MAJOR STRATIGRAPHIC UNITS IN THE BEDROCK OF FINLAND, AND AN APPROACH TO TECTONOSTRATIGRAPHIC DIVISION', p. 32.

Mattila, J. and Viola, G. (2014) 'New constraints on 1.7 Gyr of brittle tectonic evolution in southwestern Finland derived from a structural study at the site of a potential nuclear waste repository (Olkiluoto Island)', *Journal of Structural Geology*, 67, pp. 50–74. doi: 10.1016/j.jsg.2014.07.003.

McGarr, A. (2014) 'Maximum magnitude earthquakes induced by fluid injection', *Journal of Geophysical Research: Solid Earth*, 119(2), pp. 1008–1019. doi: 10.1002/2013JB010597.

Nironen - GUIDE TO THE GEOLOGICAL MAP OF FINLAND – BEDROCK 1.pdf' (2017). Available at: http://tupa.gtk.fi/julkaisu/specialpaper/sp_060_pages_041_076.pdf.

Pajunen, M. (ed.) (2008a) *Tectonic evolution of the Svecofennian crust in southern Finland: a basis for characterizing bedrock technical properties*. Espoo: Geological Survey of Finland (Special paper / Geological Survey of Finland, 47).

Pajunen, M. (ed.) (2008b) *Tectonic evolution of the Svecofennian crust in southern Finland: a basis for characterizing bedrock technical properties*. Espoo: Geological Survey of Finland (Special paper / Geological Survey of Finland, 47).

Pajunen, M. *et al.* (no date) 'TECTONIC EVOLUTION OF THE SVECOFENNIAN CRUST IN SOUTHERN FINLAND', p. 147.

Hutton, L., & Boore, D. (2005). 'THE ML SCALE IN SOUTHERN CALIFORNIA BY L. K. HUTTON AND DAVID M. BOORE'.

Miljanovic V. (2016) 'GEOTOOL SOFTWARE USER GUIDE'. Available at: https://www.ctbto.org/fileadmin/user_upload/procurement/2016/RFQ2016-0139-GEOTOOL_SOFTWARE_USER_GUIDE.pdf.

Shapiro, S. *et al.* (2010) 'Seismogenic index and magnitude probability of earthquakes induced during reservoir fluid stimulations', *The Leading Edge*, 29, pp. 304–309. doi: 10.1190/1.3353727.

Shapiro, S. *et al.* (2011) 'Magnitudes of induced earthquakes and geometric scales of fluid-stimulated rock volumes', *Geophysics*, 76, pp. WC53–WC61. doi: 10.1190/geo2010-0349.1.

Shearer, P. M. (2009) *Introduction to seismology*. 2nd ed. Cambridge University Press.

'Supplementary Materials' (2019) *Science Advances*. Available at: https://advances.sciencemag.org/content/suppl/2019/04/29/5.5.eaav7224.DC1

Trutnevyte, E. and Azevedo, I. (2018) 'Induced seismicity hazard and risk by enhanced geothermal systems: An expert elicitation approach', *Environmental Research Letters*, 13. doi: 10.1088/1748-9326/aa9eb2.

Tuija, E. *et al.* (2008) 'Fault structures in the Helsinki area, southern Finland', *Special Paper of the Geological Survey of Finland*, 2008, pp. 185–213.

Uhrhammer, R. A. and Collins, E. R. (1990) 'Synthesis of Wood-Anderson seismograms from broadband digital records', *Bulletin of the Seismological Society of America*, 80(3), pp. 702–716.

Uski, M. and Tuppurainen, A. (1996) 'A new local magnitude scale for the Finnish seismic network', *Tectonophysics*, 261(1–3), pp. 23–37. doi: 10.1016/0040-1951(96)00054-6.

Wiemer, S. *et al.* (2017) *'Good Practice' Guide for Managing Induced Seismicity in Deep Geothermal Energy Projects in Switzerland*.

Yenier*, E., Laporte, M. and Baturan, D. (2016) 'Induced-seismicity monitoring: Broadband seismometers and geophone comparison', in *SEG Technical Program Expanded Abstracts 2016*. *SEG Technical Program Expanded Abstracts 2016*, Dallas, Texas: Society of Exploration Geophysicists, pp. 5034–5038. doi: 10.1190/segam2016-13970947.1.

Zang, A. *et al.* (2014) 'Analysis of induced seismicity in geothermal reservoirs – An overview', *Geothermics*, 52, pp. 6–21. doi: 10.1016/j.geothermics.2014.06.005.

12 APPENDIX

12.1 APPENDIX A

Appendix A, Full list of the seismic stations used, involving the stations of the monitoring network and used permanent seismic network stations. The non-operational WT array is also involved in the list.

Station name	Longitude (°N)	Latitude (°E)	Elevation (km)
UNIV	60.2040	24.9626	-0.307
MALM	60.1863	24.6806	-0.329
MUNK	60.1557	24.9310	-0.290
LASS	60.2334	24.8896	-0.343
LEPP	60.2177	24.8286	-0.337
TVJP	60.1535	24.8080	-0.333
RUSK	60.2024	24.9166	-0.309
ELFV	60.2019	24.8186	-0.260
TAPI	60.1700	24.7917	-0.238
OTRA	60.1863	24.8373	-0.666
TAGC	60.1963	24.7880	-1.148
MURA	60.2005	24.8588	-1.198
HEL1	60.1771	24.8825	0.005
HEL2	60.1880	24.8314	0.005
HEL3	60.1732	24.8244	0.005
HEL4	60.2454	24.8061	0.005
HEL5	60.1173	24.7388	0.005
ZAK	60.205930	24.838090	0.010
DID	60.185330	24.855640	0.010
DT00	60.224860	25.048590	0.010
DT01	60.249190	25.102680	0.010
EV00	60.204610	24.819440	0.010
EV01	60.204660	24.819790	0.010
EV02	60.204790	24.820060	0.010
EV03	60.204720	24.820590	0.010
EV04	60.204740	24.820930	0.010
EV05	60.204350	24.819560	0.010
EV06	60.204460	24.819970	0.010
EV07	60.204560	24.820470	0.010
EV08	60.204560	24.820740	0.010
EV09	60.204520	24.821190	0.010
EV10	60.204230	24.819540	0.010
EV11	60.204300	24.819960	0.010
EV12	60.204330	24.820590	0.010
EV13	60.204360	24.820940	0.010
EV14	60.204320	24.821330	0.010
EV15	60.203870	24.819870	0.010

EV16	60.204130	24.820080	0.010
EV17	60.204070	24.820700	0.010
EV18	60.204130	24.821050	0.010
EV19	60.204120	24.821540	0.010
EV20	60.203770	24.820470	0.010
EV21	60.203860	24.820810	0.010
EV22	60.203920	24.821300	0.010
EV23	60.203960	24.821530	0.010
KUN	60.223810	24.767110	0.010
LTS	60.169580	24.856120	0.010
MKK	60.194180	24.772070	0.010
PK00	60.153390	24.858770	0.010
PK01	60.153100	24.858130	0.010
PK02	60.152820	24.858110	0.010
PK03	60.153210	24.857520	0.010
PM00	60.221040	24.856420	0.010
PM01	60.221260	24.856180	0.010
PM02	60.220720	24.855980	0.010
PM03	60.221030	24.857010	0.010
HAN	60.163620	24.834700	0.010
RAD	60.184350	24.837380	0.010
RS00	60.179890	24.734020	0.010
RS01	60.179570	24.733770	0.010
RS02	60.179860	24.733230	0.010
RS03	60.179900	24.732640	0.010
SS00A	60.183550	24.883130	0.010
SS00B	60.183980	24.882070	0.010
SS01	60.184060	24.882410	0.010
SS02	60.183980	24.882900	0.010
SS03	60.184030	24.883250	0.010
SS04	60.184030	24.883550	0.010
SS05	60.183820	24.881750	0.010
SS06	60.183880	24.882250	0.010
SS07	60.183840	24.882550	0.010
SS08	60.183830	24.882940	0.010
SS09A	60.183850	24.883490	0.010
SS09B	60.183820	24.883590	0.010
SS10	60.183570	24.881810	0.010
SS11	60.183640	24.882100	0.010
SS12	60.183650	24.882620	0.010
SS13	60.183630	24.882920	0.010
SS14	60.183650	24.883410	0.010
SS15	60.183400	24.881580	0.010
SS16	60.183420	24.882190	0.010
SS17	60.183380	24.882510	0.010
SS18	60.183440	24.883030	0.010

SS19	60.183510	24.883460	0.010
SS20	60.183210	24.881530	0.010
SS21	60.183180	24.882130	0.010
SS22	60.183150	24.882570	0.010
SS23A	60.183200	24.883010	0.010
SS23B	60.183180	24.883170	0.010
SS24	60.183330	24.883370	0.010
TL00	60.159080	24.787780	0.010
TL01	60.159130	24.788150	0.010
TL02	60.159180	24.788580	0.010
TL03	60.159180	24.788920	0.010
TL04	60.159150	24.789300	0.010
TL05	60.158850	24.788240	0.010
TL06	60.158810	24.788590	0.010
TL07	60.159030	24.788600	0.010
TL08	60.159020	24.789010	0.010
TL09	60.158940	24.789360	0.010
TL10	60.158660	24.788130	0.010
TL11	60.158640	24.788510	0.010
TL12	60.158590	24.788890	0.010
TL13	60.158790	24.789080	0.010
TL14	60.158800	24.789330	0.010
TL15	60.158460	24.788160	0.010
TL16	60.158310	24.788290	0.010
TL17	60.158530	24.788570	0.010
TL18	60.158710	24.789330	0.010
TL19	60.158520	24.789530	0.010
TL20	60.158240	24.788580	0.010
TL21	60.158330	24.789020	0.010
TL22	60.158360	24.789530	0.010
WEG	60.179540	24.794440	0.010
WT00	60.160760	24.767270	0.010
WT01	60.160570	24.767400	0.010
WT02	60.161020	24.766870	0.010
WT03	60.160910	24.767270	0.010
WT04	60.161000	24.765750	0.010
WT05	60.160660	24.766080	0.010
WT06	60.160720	24.766790	0.010
WT07	60.160640	24.765670	0.010
WT08	60.160310	24.766300	0.010
WT09	60.160840	24.765490	0.010
WT10	60.161160	24.766910	0.010
WT11	60.160860	24.766280	0.010
WT12	60.160500	24.766930	0.010
WT13	60.161160	24.766350	0.010
WT14	60.160980	24.766120	0.010

WT15	60.160360	24.767370	0.010
WT16	60.160510	24.765750	0.010
WT17	60.160980	24.766640	0.010
WT18	60.160830	24.765910	0.010
WT19	60.160530	24.766350	0.010
WT20	60.161090	24.767300	0.010
KPF	61.8337	22.0704	0.082
RUF	61.4247	28.9497	0.125
MEF	60.2172	24.3958	0.0550
NUR	60.5090	24.6514	0.1020
PVF	60.5451	25.8616	0.0100
FIA1	61.4445	26.0793	0.1380
ARBE	59.4365	25.9841	0.071
KAF	62.1112	26.3095	0.1950
KEF	62.1664	24.8706	0.2150
RAF	61.0227	21.7679	0.000
VJF	60.5388	27.5550	0.034
EE08	58.65724	25.24031	0.037
EE01	59.20648	23.62229	0.008

12.2 APPENDIX B

Appendix B, Full list of earthquakes used in the study involving their magnitudes, origin times and hypocenter locations.

Event PREFIX	Manual event magnitude (ML)	Date (mm:dd)	Time (hh:tt)	Time (s)	Longitude (°N)	Latitude (°E)	Depth (km)
2018162052548	1,45	0611	0526	48.7	60.191	24.834	5.6
2018171001230	1,34	0620	0013	04.0	60.194	24.840	6.1
2018171232614	1,66	0620	2327	15.1	60.193	24.841	6.1
2018172175518	1,34	0621	1756	18.6	60.195	24.839	6.0
2018174085934	1,25	0623	0900	01.9	60.193	24.842	6.1
2018180040100	1,70	0629	0402	45.1	60.194	24.843	6.3
2018180094138	1,46	0629	0942	38.8	60.194	24.843	6.2
2018181065239	1,47	0630	0653	07.8	60.194	24.839	6.1
2018186070100	1,48	0705	0701	55.6	60.193	24.842	6.0
2018187084836	1,43	0706	0849	36.3	60.194	24.843	6.2
2018188173124	1,49	0707	1732	24.9	60.191	24.832	5.6
2018189173537	1,84	0708	1736	37.0	60.192	24.842	6.1
2018193142500	1,37	0712	1425	19.4	60.193	24.840	6.1
2018194133411	1,44	0713	1335	11.6	60.193	24.842	6.1
2018197172535	1,79	0716	1726	02.9	60.196	24.837	6.1
2018199104200	1,39	0718	1043	18.0	60.194	24.844	6.2
2018199224500	1,34	0718	2245	37.8	60.193	24.842	6.1
2018200105407	1,29	0719	1055	07.4	60.192	24.840	6.0
2018200105452	1,53	0719	1055	53.0	60.193	24.842	6.1
2018204220258	1,35	0723	2203	58.4	60.196	24.838	6.2
2018220155710	1,22	0808	1558	14.9	60.192	24.841	6.0